Fluorinated amphiphilic Poly(β-Amino ester) nanoparticle for highly efficient and specific delivery of nucleic acids to the Lung capillary endothelium

Zicheng Deng [a], Wen Gao [a], Fatemeh Kohram [a], Enhong Li [a], Tanya V. Kalin [b], Donglu Shi [c,*], Vladimir V. Kalinichenko [a,d,**]

[a] Phoenix Children's Health Research Institute, Department of Child Health, University of Arizona College of Medicine-Phoenix, Phoenix, AZ, 85004, USA
[b] Division of Pulmonary Biology, Cincinnati Children's Hospital Medical Center, Cincinnati, OH, 45229, USA
[c] The Materials Science and Engineering Program, College of Engineering and Applied Science, University of Cincinnati, Cincinnati, OH, 45221, USA
[d] Division of Neonatology, Phoenix Children's Hospital, Phoenix, AZ, 85016, USA

ARTICLE INFO

ABSTRACT

Endothelial cell dysfunction occurs in a variety of acute and chronic pulmonary diseases including pulmonary hypertension, viral and bacterial pneumonia, bronchopulmonary dysplasia, and congenital lung diseases such as alveolar capillary dysplasia with misalignment of pulmonary veins (ACDMPV). To correct endothelial dysfunction, there is a critical need for the development of nanoparticle systems that can deliver drugs and nucleic acids to endothelial cells with high efficiency and precision. While several nanoparticle delivery systems targeting endothelial cells have been recently developed, none of them are specific to lung endothelial cells without targeting other organs in the body. In the present study, we successfully solved this problem by developing non-toxic poly(β-amino) ester (PBAE) nanoparticles with specific structure design and fluorinated modification for high efficiency and specific delivery of nucleic acids to the pulmonary endothelial cells. After intravenous administration, the PBAE nanoparticles were capable of delivering non-integrating DNA plasmids to lung microvascular endothelial cells but not to other lung cell types. IVIS whole body imaging and flow cytometry demonstrated that DNA plasmid were functional in the lung endothelial cells but not in endothelial cells of other organs. Fluorination of PBAE was required for lung endothelial cell-specific targeting. Hematologic analysis and liver and kidney metabolic panels demonstrated the lack of toxicity in experimental mice. Thus, fluorinated PBAE nanoparticles can be an ideal vehicle for gene therapy targeting lung microvascular endothelium in pulmonary vascular disorders.

1. Introduction

Endothelial dysfunction contributes to a wide range of severe pulmonary vascular diseases such as Pulmonary hypertension, pneumonia, idiopathic pulmonary fibrosis, cystic obstructive pulmonary disease, bronchopulmonary dysplasia (BPD) and alveolar capillary dysplasia with misalignment of pulmonary veins (ACDMPV). The transcription factor FOXF1 plays a key role in pulmonary vascular development and endothelial repair after lung injury. Mutations in the FOXF1 gene has been associated with lung ACDMPV, a fatal congenital lung disorder, hypoplasia, and paucity of alveolar capillaries in newborns and infants [1–5]. Nanoparticle delivery of FOXF1 has promise for ACDMPV treatment.

Recent studies have developed innovative drugs for treatment of chronic obstructive pulmonary disease (COPD) [6], however, there is still a critical need for versatile platforms that can deliver gene payloads and drugs to pulmonary endothelium with high efficiency and precision. Although viral vectors have been widely used for gene delivery in

preclinical studies, there are still major concerns with the use of viral vectors such as high biosafety risks, adverse immune responses, low payload capacity, and limited clinical translation due to difficulties in vector production [7–10]. In recent years, non-viral gene delivery systems were developed to address these limitations for gene therapy.

Nanoparticle delivery systems have been shown to serve as effective non-viral gene delivery vehicles with great potential in biomedical applications, including cancer gene therapy and the development of SARS-CoV-2 vaccines [11–15]. Nanoparticle-based gene therapies for pulmonary diseases can usually be divided by their administration routes, including pulmonary administration through airways and systemic administration through intravascular route. Pulmonary administration has been widely used because it delivers therapeutics directly to the lung via the trachea, which can increase the local accumulation of nanoparticles. But this route is affected by mucous and epithelial barriers, therefore diverting the nanoparticles to the epithelium. For endothelial targeting, the nanoparticles are delivered via systemic administrations to avoid epithelial barrier. However, the first pass metabolism may cause high transfection efficiencies in other organs resulting in low nanoparticle delivery to the lung endothelium [16]. To treat pulmonary vascular disorders, it is necessary to develop a nanoparticle delivery system that can efficiently deliver the cargo to the lung while targeting only endothelial cells. Recently, several nanoparticle delivery systems have been developed for pulmonary endothelial targeting using specific endothelial markers such as angiotensin-converting enzyme (ACE) [17], plasmalemmal Vesicle-Associated Protein (Plvap/PV1) in caveolae [18], and cell adhesion molecules PECAM and ICAM [19,20]. In vivo, certain drugs, imaging agents, and other biologics have been altered by attaching specific endothelial ligands. These modifications enable the targeting of these substances specifically to the pulmonary endothelium [21–24]. These determinants enable a unique control of endothelial intracellular delivery of nucleic acids and other biologics [25,26]. Furthermore, ligand-mediated anchoring to endothelial determinants has been shown to mediate intracellular delivery in a controlled fashion [27,28]. Monomolecular PECAM ligands are not effectively internalized by endothelial cells [29], However, through the utilization of multivalent constructs and carriers specifically designed to target PECAM, these substances can enter the cells using an alternative endocytic pathway [30]. ICAM-1-targeted nanoparticles can efficiently induce internalization [31]. On the other hand, biomechanical factors have been shown to modulate the intracellular uptake of PV1-targeted nanogels and ferritin nanocages [32,33]. The uptake of ligand-targeted carriers can also be modulated by hydrodynamics [34], nanoparticle geometry [35], nanoparticle configuration [36], and biomechanical features of the nanoparticles [37]. The use of targeting ligands is not the sole strategy in pulmonary delivery. Min, Q. et al. developed a lipid nanoparticle formulation for mRNA delivery, demonstrating efficient pulmonary transfection compared to other nanoparticle formulations [38]. In our previous work, we developed a polymeric-based gene delivery system based on biological fatty acids and modified hyperbranched polyethylenimine (PEI), which is capable of delivering non-integrating plasmids to the lung endothelium without targeting other cell types in the adult lung [39,40]. However, this nanoparticle system also targets endothelial cells of other organs, such as heart, liver and kidney [4], limiting potential clinical applications of the nanoparticles in lung diseases. The nanoparticle delivery system for specific delivery to the lung endothelium without targeting other organs has not been developed yet.

Poly(β-amino) esters (PBAEs) refer to a wide range of polymers that are synthesized using the Michael Addition of amine groups to diacrylates. PBAEs are considered to be promising polymers in biomedical applications owing to their excellent biocompatibility and biodegradability [41–44]. As cationic polymer structures, PBAE-based nanoparticles have shown high potential for gene delivery [45–48]. Recent studies showed effective delivery of mRNAs and DNAs through pulmonary or systemic delivery using the polymer-lipid nanoparticles combined with PBAEs and lipid molecules via microfluidic devices [49–52].

Polyplexes were also used in recent studies for gene delivery with considerable transfection efficiency, and they do not require extra lipid molecules or devices for their straightforward synthesis. However, these PBAE polyplexes required pulmonary administration to achieve high pulmonary accumulation [42,53]. Fluorination has been reported as an effective strategy to improve gene delivery efficiency in recent studies [54,55]. The fluorous ligands can boost the binding affinity between cationic polymers and nucleic acids, and self-assembly into stable nanoparticles [56]. Fluorinated vectors were reported to have a better serum tolerance and lower cytotoxicity [57], and published studies showed that the fluorination can promote membrane permeability which contribute to endocytosis, endosomal escape, and gene release [58].

In the present studies, we developed a facile synthesis of the polymer with hydrophobic PBAE backbones and capped with the hydrophilic low molecular polyethylenimine (PEI) and poly (ethylene glycol) (PEG). This amphiphilic structure provides excellent nanoparticle colloidal stability and cationic density for gene encapsulation and delivery. Furthermore, we used fluorous ligands to improve the performance of the PBAE nanoparticles and achieve lung-specific delivery via the systemic intravenous route. IVIS whole body imaging of experimental mice and flow cytometry analysis of multiple organs demonstrated specific gene delivery to lung microvascular endothelial cells without targeting other organs. Fluorination of PBAE was required for lung-specific endothelial delivery since the nanoparticles without fluorination did not exhibit lung specificity. Altogether, fluorinated PBAE nanoparticles have promise for gene therapying pulmonary diseases associated with endothelial disfunction.

2. Materials and methods

2.1. Materials and DNA plasmids

All materials for PBAEs synthesis were purchased from Sigma-Aldrich (St. Louis, MO, USA) including Bisphenol A ethoxylate (EO/phenol) diacrylate (D1), 4,4′-Trimethylenedipiperidine (A1), 6-amino-1-hexanol (A2), polyethylenimine (PEI, Mn ~600) (C1), poly(ethylene glycol) amine (PEG, Mn ~2000) (C2), Pentadecafluorooctanoyl chloride (F1), Pentafluoropropionic anhydride (F2), 1H,1H,2H,2H-Perfluorodecyl acrylate (F3) Pentafluoropropionic anhydride (F4). D-Luciferin, Potassium Salt was purchased from Gold Biotechnology (St. Louis, MO, USA). mCherry was cloned into the Multiple Cloning Site (MCS) of the pMC.EF1α-MCS-SV40polyA Parental Plasmid (PP) to produce mCherry-PP (Minicircle DNA technology, System Biosciences). Briefly, mCherry-PPs were transfected into ZYCY10P3S2T *E. coli* Minicircle producer competent cells (MPCs) which harbored an arabinose-inducible system to express ΦC31 integrase and the I-SceI endonuclease simultaneously. Following propagation of PPs in MPCs, arabinose was added to the media to induce ΦC31 integrase and the I-SceI endonuclease expression. In this process, ΦC31 integrase mediated an intramolecular recombination between *cis*-positioned attP and attB sites on PPs, creating the MC and a bacterial backbone. I-SceI endonuclease digested the bacterial backbone through the 32 copies of I-SceI restriction sites, incorporated in the DNA, yielding clean MC DNA. DyLight 650 NHS ester, SnakeSkin™ Dialysis Tubing, 3.5K MWCO were obtained through ThermoFisher Scientific (Waltham, MA, USA). Cell culture Cell Counting Kit-8 (CCK-8) was purchased from Apexbio (Houston, TX, USA). CMV-turboGFP plasmid was purchased from Evrogen. gWiz luciferase-encoding DNA plasmid was purchased from Aldevron (Fargo, ND, USA). All antibodies used for flow cytometry and immunostaining were purchased from BioLegend (San Diego, CA, USA), BD Bioscience (Franklin Lakes, NJ, USA), MilliporeSigma (Burlington, MA, USA) and ThermoFisher (eBioscience) and listed in supplemental table s1.

2.2. PBAE nanoparticle synthesis and characterization

The PBAE polymer backbone was synthesized and capped in anhydrous dimethylsulfoxide (DMSO) at various temperatures with different monomer ratios. Briefly, the A2 monomer (primary amine) and D1 monomer (diacrylates) were mixed at 90 °C for 24 h. The A1 monomer (secondary amine) was added to the mixture at 50 °C for another 24 h. The backbone polymers were diluted in DMSO to a concentration of 200 mg/ml. Following the backbone synthesis, an excess of end-capping amines, including PEG and PEI, was added and reacted at 40 °C for an additional 24 h. For the fluorinated polymers, the fluorination agent was added into the capping amine at a fluorination agent with the PEI mole ratio of 1:4. The PBAE polymers were stored at −20 °C.

Before assembling with plasmid, PBAE polymers were dialyzed against deionized H_2O using a 3.5 kDa membrane for 2 days to remove the excess of capping agents and DMSO. The product polymers were dissolved in a 25 mM HEPES buffer (pH = 7.4) at a concentration of 10 mg/ml. To prepare DNA-encapsulated polyplex nanoparticle, DNA and PBAEs were simply mixed by pipette thoroughly. For the fluorescent nanoparticles, polymers were fluorescently tagged by mixing the NHS-functionalized fluorophores with polymers at room temperature using a vortex. The nanoparticles were allowed to rest at room temperature for at least 30 min and used no later than 4 h following formulation.

The hydrodynamic diameter and surface potential of the PBAE nanoparticles were determined by dynamic light scattering (DLS) using a Zetasizer Nano-ZS (Malvern, Malvern, UK). The ^{1}H NMR (nuclear magnetic resonance) was taken in deuterated chloroform on a Bruker AV 400 MHz spectrometer (Bruker, MA, USA). Gel electrophoresis was performed using Tris/borate/ethylenediaminetetraacetic acid (TBE)-based agarose gels (0.8% w/v, 0.5 × TBE) at 120 V and imaged using a Bio-Rad Gel Doc.

2.3. In vitro transfections and cytotoxicity assay

The HEK-293T cell line was cultured in Dulbecco's Modified Eagle Medium (DMEM, Gibco) supplemented with 10% heat-inactivated fetal bovine serum (FBS, Gibco) and 1% v/v Penicillin Streptomycin (Invitrogen) in a controlled environment at 37 °C and 5% CO_2. For green fluorescent protein (GFP) transfection, the cells were seeded onto a 96-well polystyrene tissue culture plate 24 h before transfection. Typically, the GFP plasmid and polymer were diluted into 100 ng/μl and 1 μg/μl, separately, followed by mixing in the OPTI-MEM (Gibco) at certain ratios. Nanoparticles encapsulated with GFP plasmid were added to the cells at a concentration of 100 ng DNA/well. After 4 h incubation, the medium was replaced with fresh DMEM medium with 10% FBS, and the plate was incubated for an additional 48 h. The GFP intensity was registered by a Flexstation 3 Multi-Mode Microplate Reader (Molecular Devices, CA, USA). The microscopic images of the GFP expression with different nanoparticle formulation were taken by EVOS M7000 fluorescence microscope. For confocal microscopy, 8 chamber-slides were used for cell culture and immunostaining. The cells were fixed using 4% PFA (Paraformaldehyde, Electron Microscopy Sciences, Hatfield, PA, USA), and the cell nuclei were counterstained with DAPI (4′, 6-diamidino-2-phenylindole, blue). The images were captured using a Nikon A1R GaAsP inverted confocal microscope. The in vitro cell viability was assessed using the Cell Counting Kit. The nanoparticles were diluted to different concentrations and added to cells for 24 h. The assay absorbance was measured at a wavelength of 450 nm using a Microplate Reader.

2.4. Animal studies

All animal experiments were approved by the Institutional Animal Care and Use Committee. NIH guidelines for laboratory animal care and safety were strictly followed. Adult CD1 and SKH-1 mice (Charles River Laboratories, 8–12 weeks) were used for animal studies. For the lung targeting and nanoparticle localization experiments, CD1 mice were intravenously injected with DyLight 650 labeled nanoparticles and the cells from dissected lung tissue were harvested 24 h after the nanoparticle injection. Luciferase reporter activity was measured by using the IVIS Lumina III Imaging system and the IVIS Spectrum CT In Vivo Imaging System (PerkinElmer, MA, USA). For ex-vivo IVIS imaging, CD1 mice were injected intraperitoneally with 200 μL D-luciferin (30 mg/mL) 48 h after the nanoparticle administration. The mice were sacrificed 10 min after the luciferin injection and internal organs (heart, liver, spleen, lung, and kidney) were collected for luminescence imaging. The SKH-1 hairless mice were used for in-vivo IVIS image. The mice were injected intraperitoneally with D-luciferin as described [51], and the whole-body imaging was performed 10 min following the D-luciferin injection. The luminescence intensity was quantified using Living Image software.

2.5. Flow cytometry

Lungs from CD1 mice were digested in DMEM medium supplemented with 0.5 mg/mL and DNase, 100 μg mL^{-1} liberase. The red blood cells were removed using ACK lysis buffer for 5 min on ice. Nonspecific background was blocked in autoMACS® Running Buffer with TruStain FcX™ (anti-mouse CD16/32) antibody (BioLegend, 101320). Cells were then stained with CD31 Ab labeled with eF450, CD45 Ab labeled with AF700, CD140a Ab labeled with PE Cy7, CD326 Ab labeled with PerCP-Cy5.5 (Supplemental table s1). Dead cells were stained with 7-AAD Viability Dye (BioLegend, 420404). CD31$^+$ CD45$^-$ CD326-CD140a-cell population was identified as endothelial cells. CD45$^+$ CD31$^-$ CD326- CD140a-cell population was identified as hematopoietic cells. CD326+ CD31$^-$ CD45$^-$ CD140a-cells were identified as epithelial cells, CD140a + CD31$^-$ CD45$^-$ CD326-cells as fibroblasts, and CD140a-CD31$^-$ CD45$^-$ CD326-as lineage-negative cells, which include pericytes, smooth muscle and other respiratory cell types [39]. FACS analysis was performed using a BD Biosciences LSR II cytometry and data were analyzed by FlowJo software.

2.6. Immunofluorescence

Lungs from CD1 mice were collected and cryosections (7 μm) were prepared for immunofluorescence as described previously [39]. The rat anti-CD31 and mouse anti-αSMA antibodies were used to identify endothelial and smooth muscle cells, respectively. After primary antibodies, cells were incubated with the donkey anti-mouse antibodies labeled with AF594 and donkey anti-mouse antibodies labeled with AF488. Fluorescence images were captured by a Zeiss Axioplan2 microscope and Nikon A1R confocal microscope. Analysis was performed using Imaris software, and the quantification of nanoparticles in the images was performed using imageJ software as reported before [59].

2.7. Clinical toxicity evaluation

Blood and serum were collected from the mice 5 days after the nanoparticle injection. Ten CD1 mice were used for the toxicology study (5 for the experimental group treated with nanoparticle at NP:DNA = 50:1 ratio, 5 for the control group treated with glucose injection solution). The peripheral blood was collected in MINICOLLECT® K2E K2EDTA blood sample tubes. MiniCollect® TUBE 0.8 ml CAT Serum Separator (Greiner Bio-One, Kremsmünster, Austria) was used to prepare the blood serum. Collected samples were analyzed by IDEXX Bio-Analytics (North Grafton, MA, USA) for clinical chemistry and hematology of the peripheral blood.

2.8. Statistics

Unpaired, two-tailed student's t-test in Graphpad Prism was used to determine statistical significance. P values < 0.05 were considered

significant. All data were shown as mean ± SD for groups of at least three replicates.

3. Results

3.1. PBAEs polymer synthesis, optimization and characterization

We used a library of monomers for PBAE polymer synthesis and fluorination (Supplemental Fig. S1A). The PBAE polymer backbones were synthesized using a step-growth polymerization via Michael addition between the diacrylates and amines. The hydrophobic PBAE backbones were further capped with hydrophilic capping agents to form amphiphilic PBAE polymer chains (Fig. 1A). The characterization data on the PBAEs are shown in the Supplemental materials including the typical chemical structures and ^1H NMR spectrum of the starting materials (Supplemental Fig. S2 A-C), and the synthesized polymers (Supplemental Fig. S2 D-E). Resonance signals from terminal acrylate groups on the D1 (Bisphenol A ethoxylate diacrylate) and uncapped PBAE backbones were observed at 5.8 ppm–6.5 ppm (Supplemental Fig. S2A and Fig. S2D). These resonance peaks disappeared upon capping with C1 (PEI) and C2 (PEG), indicating the successful covalent attachment of these capping agents to the PBAE backbones via Michael Addition (Fig. S2E). Furthermore, the characteristic peaks from A1 (4,4′-Trimethylenedipiperidine, Fig. S2B) and A2 (6-amino-1-hexanol, Fig. S2C) are present in the products after polymerization (Fig. S2D and Fig. S2E), indicating successful synthesis of PBAE polymers. The cationic amphiphilic PBAEs can self-assemble with the nucleic acid and form stable nanoparticles in aqueous medium (Fig. 1 B).

To exclude ineffective formulations and select the most effective nanoparticles for further in vivo testing, a set of initial in vitro transfection experiments were performed using HEK-293T cells. Variations of the polymer formulations influenced the transfection efficiency (Fig. 2A). The changes in A1 to A2 ratio significantly altered the transfection efficiency of the nanoparticles. For nanoparticles with more A1 than A2, the gelation of PBAE polymers caused failure in the nanoparticle synthesis. PBAEs with only A2 in the backbones yielded lower transfection efficiencies compared to PBAEs containing both A1 and A2 in the backbone. Interestingly, incorporation of PEG (3–6%) in capping agents increased the transfection efficiency as shown in Fig. 2A (P1, P11, and P21 polymers without PEG capping; P2, P12, and P22 polymers with 3% PEG capping; and P3, P13, and P23 polymers with 6% PEG capping, Supplemental Table S2).

To investigate the influence of fluorous ligands, the PBAE formulations with the highest transfection efficiency (P13 and P22) were used for fluorination. The F1 fluorination increased the transfection efficiency, especially for the P22 polymer (Fig. 2B–C). However, the transfection efficiency was lower if the length of the fluorous ligands was further increased (F3 and F4). The gel electrophoresis analysis was used to determine the w/w ratio required to stabilize DNA in the nanoparticles (Fig. 2D). PBAEs with only A2 in the backbone and capped with PEI encapsulated all the DNA at a polymer to DNA mass ratio of 2 (P1). After using A1 in the formulation (P21) and 3% of PEG in capping agents
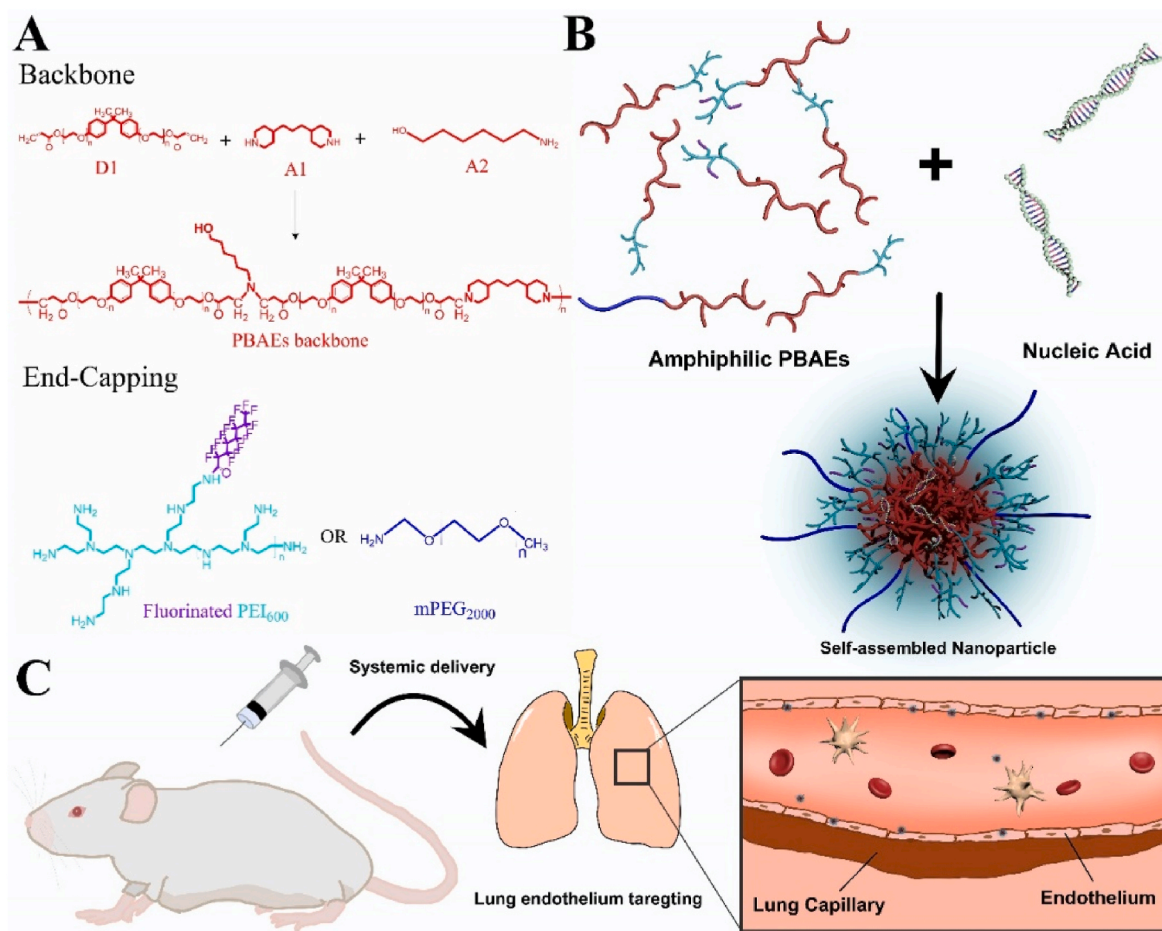
Fig. 1. Overview of the PBAE nanoparticle synthesis and gene delivery to the pulmonary endothelium. (A) Schematic of the PBAE backbone synthesis with hydrophobic monomers (red) and the hydrophilic capping agents polyethylenimine (cyan), polyethylene glycol (blue) and fluorous ligands (purple); (B) Schematic of the PBAEs nanoparticle structure. Amphiphilic PBAEs polymers are binding the nucleic acid to form nanoparticles with hydrophilic surfaces and hydrophobic cores. (C) The PBAE nanoparticles were synthesized to deliver DNA plasmid to pulmonary endothelial cells after intravenous injection.

Fig. 2. The effect of fluorination of PBAE polymer on the size, charge and transfection efficiency of the nanoparticles. (A) *In vitro* transfection efficiency of PBAE nanoparticles with different formulations and polymer to DNA mass ratios. (B) The influence of fluorous ligands on the *in vitro* transfection efficiency of the PBAE P13. (C) The influence of fluorou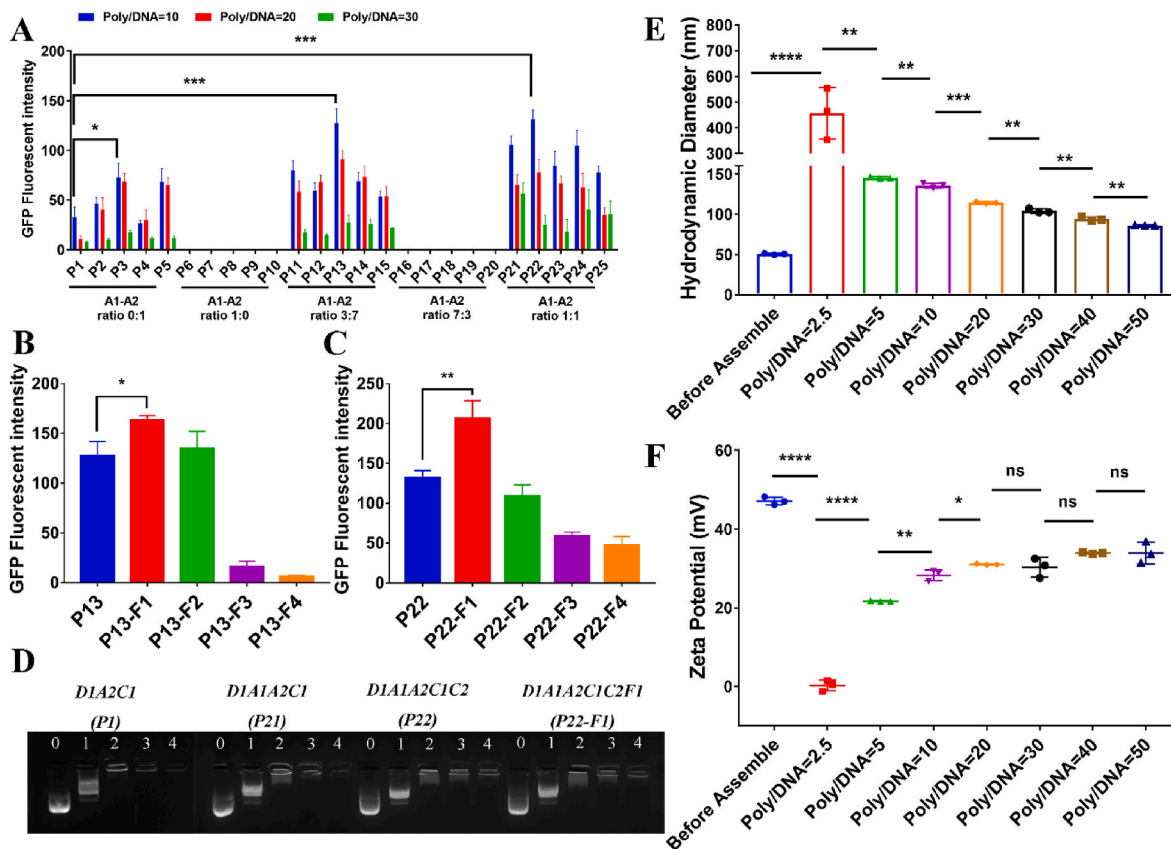s ligands on the *in vitro* transfection efficiency of the PBAE P22. (D) Gel electrophoresis analysis of plasmid DNA bound to the PBAE P1, P21, P22 and P22–F1 at different polymer to DNA mass ratios. (E) The hydrodynamic diameter of the PBAE P22–F1 nanoparticles at different polymer to DNA mass ratios. (F) The zeta potential of the PBAE P22–F1 nanoparticles at different polymer to DNA mass ratios.

(P22), the required mass ratio for DNA full encapsulation was increased to 3. The fluorination (P22–F1) did not influence DNA encapsulation into PBAE nanoparticles (Fig. 2D). The size and surface charge of the P22–F1 PBAEs with different nanoparticle to DNA mass ratio (NP/DNA) were determined by dynamic light scattering. Before assembling with DNA, the average hydrodynamic size of polymer nanoparticles was 50 nm, however, the nanoparticle size was significantly increased after assembly with DNA (Fig. 2E). When the polymer to DNA ratio was set at 2.5, the nanoparticles were unstable and aggregated into large particles (Fig. 2F), most likely, due to the neutral surface charge, which is known to decrease electrostatic repulsive forces between the nanoparticles [60]. After the polymer to DNA mass ratio reached 5, the nanoparticle size was decreased to 150 nm and the surface charge was increased to 20 mV (Fig. 2E–F). The nanoparticle size further decreased to 90 nm after increasing the polymer/DNA ratio to 50 (Fig. 2E).

Fluorescence microscopy and flow cytometry were used to measure the transfection efficiency of PBAE nanoparticles after the PEG modification and fluorination. HEK-293T cells were transfected with nanoparticles containing the CMV-GFP reporter plasmid. The nanoparticles containing both PEG and fluorous ligands exhibited brighter GFP fluorescence compared to nanoparticles containing either PEG or fluorous ligands (Fig. 3A). We used flow cytometry to quantify the transfection efficiency of the nanoparticles in HEK-293T cells *in vitro* (Fig. 3B–D). Compared to nanoparticles without PEG, the nanoparticles containing PEG increased the brightness of GFP in cells but did not change the percentage of transfected cells (Fig. 3C–D). In contrast, the fluorination of nanoparticles increased both the transfection efficiency and mean fluorescence intensity (MFI) (Fig. 3C–D). There were no significant changes in cell viability after the PEG modification and fluorination of

the PBAE nanoparticles (Fig. 3E). Consistent with flow cytometry measurement, fluorescence microscopy demonstrated high efficiency of cell transfections and detected GFP in both nucleus and cytoplasm of transfected cells (Fig. 3F). The *in vitro* transfection showed that the nanoparticle can enter cells with or without serum (Fig. S3). Lipofectamine 2000 showed a similar transfection efficiency compared to P22 nanoparticles. In contrast, the fluorinated P22–F1 nanoparticles showed a significantly higher transfection efficiency compared to lipofectamine as demonstrated by an increased percentage of transfected cells and evaluated mean fluorescence intensity (Fig. S4).

Unassembled average hydrodynamic polymer size in PBS at 37 °C is 36.00 ± 1.28 nm, while the average hydrodynamic size of the assembled P22–F1 nanoparticle is 80.11 ± 7.18 nm, indicating that no disassemble or obvious aggregation occurred. The polymer size in PBS was decreased, whereas the polydispersity index (PDI) was increased compared to the polymer in water, which is highly likely due to the polyelectrolyte effect [61,62]. After addition of salt, the polymer chains begin to curl, and the statistical segment length is decreased. Since the PBAE polymer contains more than one capping agent, the variations in polymer chain conformation may lead to an increase in PDI. These results show that the nanoparticles are stable in the PBS buffer at 37 °C (Table S3). The 24-h stability study showed that the nanoparticle size slightly increased after 8 h. But the average hydrodynamic diameter and PDI of the nanoparticles did not significantly change (PDI <0.2), indicating that there is no large aggregation of the nanoparticles (Fig. S5A). Upon the addition of serum, the average hydrodynamic size of the nanoparticles decreased to 68.13 ± 0.4053 nm, while the polydispersity index (PDI) increased to 0.4939 ± 0.0079. This change is most likely attributed to the presence of numerous proteins in the serum because the
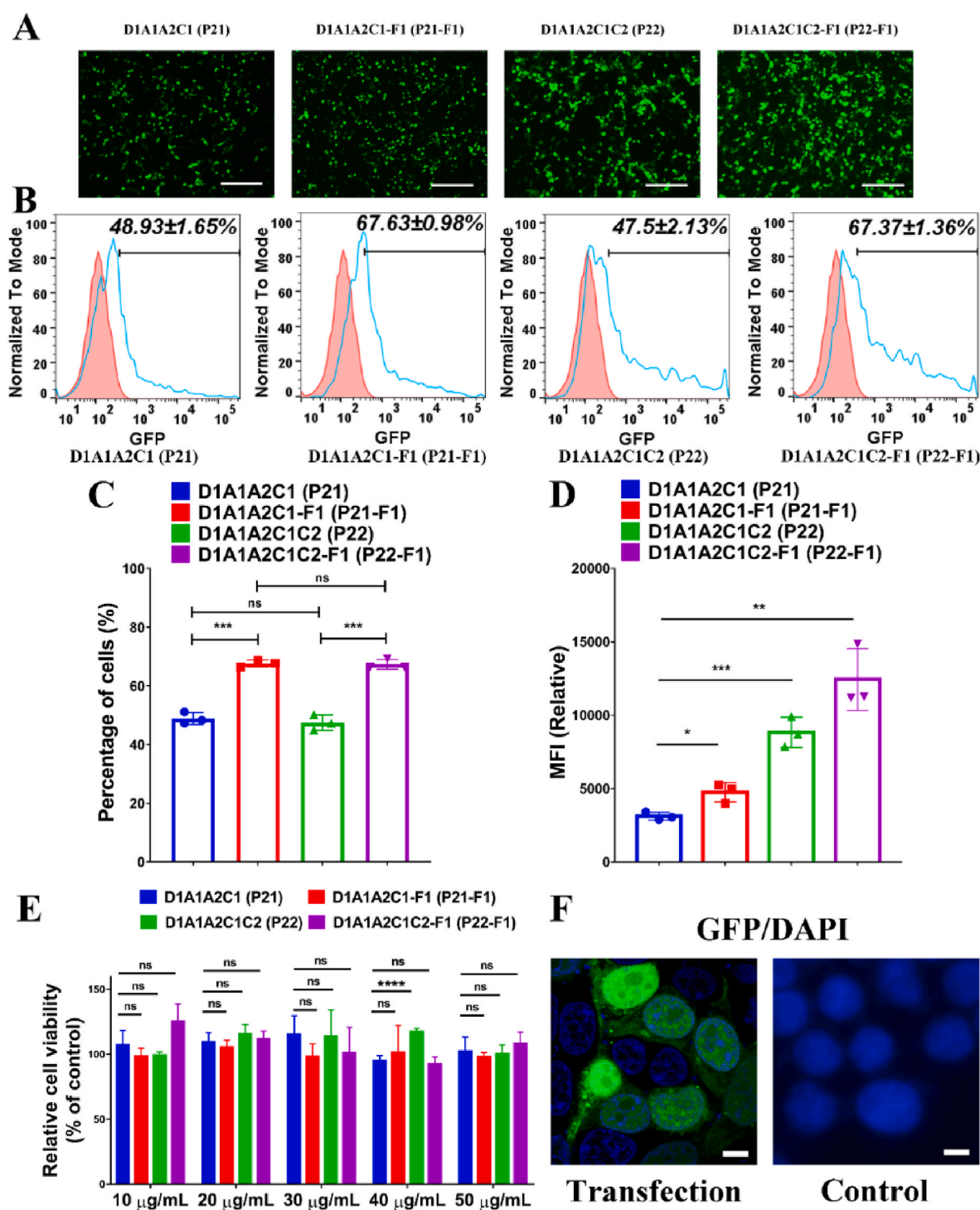
Fig. 3. The P22–F1 PBAE nanoparticles exhibit the highest transfection efficiency *in vitro*. (A) Fluorescence microscopy images of HEK-293T cells were obtained 48 h after the transfection with PBAE-GFP plasmid complexes at nanoparticle to DNA mass ratio of 10:1. (B) Flow cytometry was used to analyze HEK-293T cells 48 h after transfection with PBAE-GFP plasmid complexes at nanoparticle to DNA mass ratio of 10:1. (C) The quantification of percentages of GFP-positive (transfected) cells was performed based on flow cytometry measurements. (D) The quantification of GFP mean fluorescence intensity (MFI) of transfected cells was performed based on flow cytometry measurements. (E) Cell viability profiles of transfected cells after treatment with different concentrations of nanoparticles. (F) Representative fluorescence microscopy images show GFP (green) in transfected HEK-293T cells and untransfected cells. DAPI (blue) was used to stain cell nuclei. Scale bars: (A) 275 μm; (F) 7 μm.

sizes of serum proteins are significantly different compared to the size of the nanoparticles. The size distribution data reveals that the nanoparticles in both PBS (with or without serum) exhibit a similar peak at approximately 85 nm. Additionally, an additional peak around 7 nm is observed in the nanoparticles with serum group, which is also evident in

the serum buffer control (Fig. S5B). The presence of similar nanoparticle peaks in the size distribution indicates that the nanoparticles have a relatively uniform size. Consequently, it can be concluded that the P22–F1 nanoparticles remain stable in PBS, and the presence of serum proteins does not induce nanoparticle aggregation or disassembly at a

temperature of 37 °C.

3.2. In vivo targeting of the PBAE nanoparticles

To track the nanoparticles *in vivo*, the DyLight 650 fluorescent dye with NHS ester was used to label the PBAE polymer surface of the nanoparticles (Fig. 4A). DyLight 650-labeled nanoparticles were injected intravenously and 24 h after the injection, mouse lungs were dissected and used for flow cytometry analysis to identify the cell types containing the nanoparticles (Fig. 1C). Immunostaining for CD31, CD45, CD326 and CD140a cell surface markers identified several cell populations in the lung tissue, including fibroblasts, endothelial, epithelial,

and hematopoietic cells. Cells without these markers were identified as lineage negative cell, which contain pericytes, smooth muscle cells and other respiratory cell types (Fig. S6). The PBAE nanoparticles mainly targeted lung endothelial cells with relatively low distribution to other cell types. Compared to the nanoparticles containing only the PEI capping, the PBAE nanoparticles with PEG and F1 (P22–F1) exhibited an increased targeting efficiency of endothelial cells without significant changes in other cell types (Fig. 4B–C). Moreover, the P22–F1 nanoparticles exhibited an increased MFI (Fig. 4D), demonstrating that more endothelial cells were targeted with greater efficiency. Thus, the PEGylation and fluorination remarkably enhanced the efficiency of endothelial targeting *in vivo*.
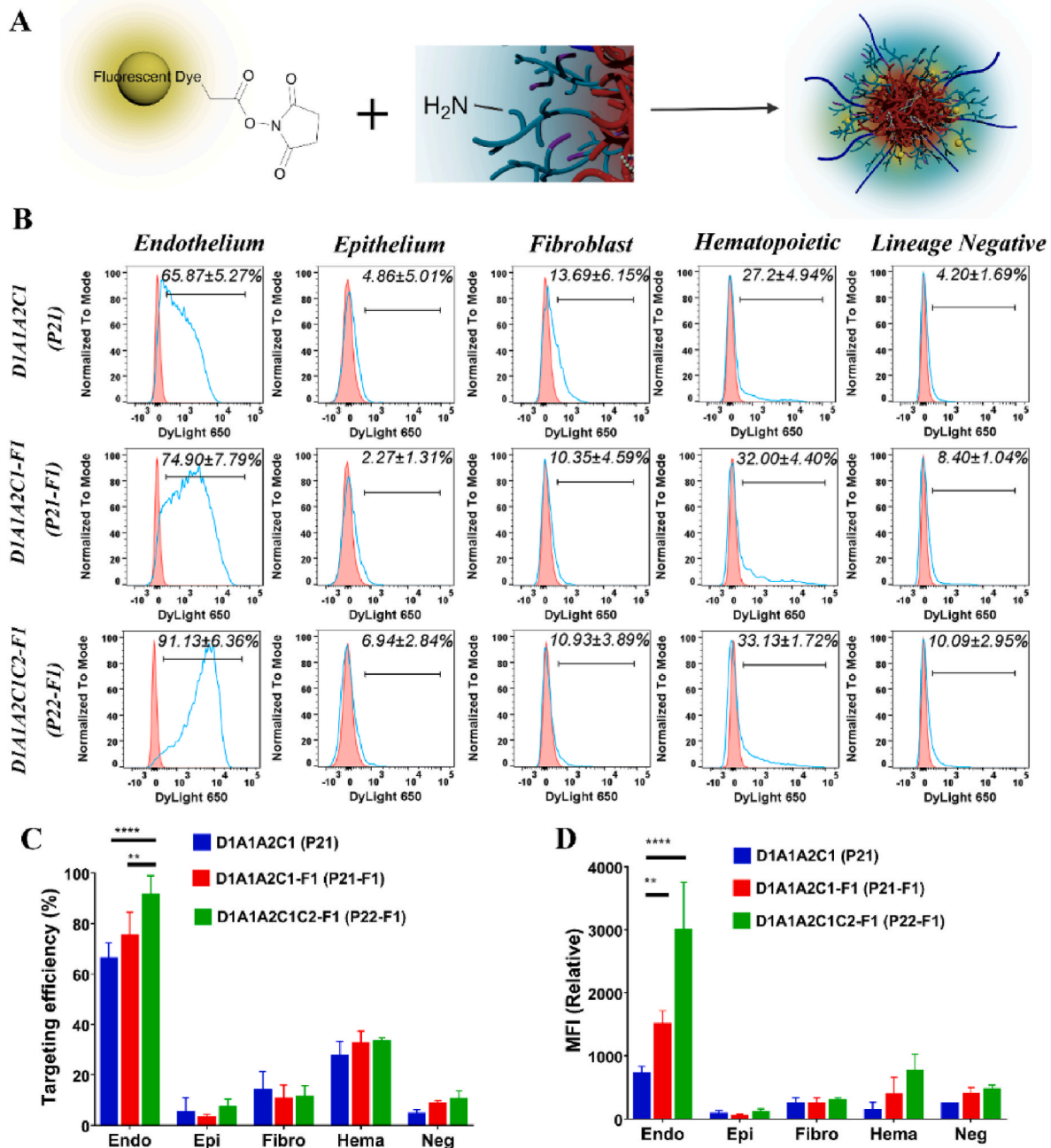
Fig. 4. The P22–F1 PBAE nanoparticles exhibit improved endothelial targeting in the lung tissue. (A) Fluorescent dye labeling of PBAE nanoparticles. (B) Flow cytometry analysis of the PBAE nanoparticle distribution (blue curve) in different respiratory cell types compared to the control (red curve). (C) Juxtaposition of cell targeting efficiency from P21, P21–F1 and P22–F1 PBAE nanoparticles (n = 3 mice were used for each group), $P < 0.0001$ is ****, $P < 0.01$ is **. (D) Juxtaposition of MFI from respiratory cells targeted with P21, P21–F1 or P22–F1 PBAE nanoparticles (n = 3 mice were used for each group), $P < 0.0001$ is ****, $P < 0.01$ is **. Abbreviations: Endo: Endothelium; Epi, Epithelium; Fibro, Fibroblast; Hema, Hematopoietic; Neg, Lineage negative.

Confocal microscopy was used to track the distribution of DyLight 650-labeled P22–F1 PBAE nanoparticles in lung tissue. To visualize the microvasculature and large pulmonary vessels, frozen lung sections from mice treated with P22–F1 PBAE nanoparticles were stained for endothelial marker CD31 (PECAM1) and smooth muscle cell marker αSMA. DyLight 650-labeled nanoparticles were highly disseminated throughout the pulmonary microvasculature in the alveolar region (Fig. 5A). In contrast, the nanoparticles were not found in endothelial cells of large pulmonary arteries and veins (Fig. 5A). Based on deconvolution of 3D high magnification confocal images followed by the cell surface reconstruction, the P22–F1 PBAE nanoparticles successfully internalized in the capillary endothelial cells in the alveolar region (Fig. 5B). No nanoparticles were detected in the control group (Fig. S7). Compared to P1, P21 and P22 nanoparticle formulations, the P22–F1

PBAE nanoparticles were the most effective in targeting lung endothelial cells (Figs. S8–S9), consistent with flow cytometry data (Fig. 4B–D). The P22–F1 PBAE nanoparticle targeting of the spleen was restricted to capillaries located in the red pulp (Fig. S10), whereas the nanoparticle targeting in the kidney was restricted to capillaries of glomeruli (Fig. S11). The P22–F1 PBAE nanoparticles detection in the heart (Fig. S12) and liver (Fig. S13) was low. The average number of the P22–F1 PBAE nanoparticles in the endothelial cells of the heart, liver, kidney, and spleen were significantly lower compared to the lung endothelial cells (Fig. S8).

Recent single-cell RNA sequencing studies demonstrated that lung capillary endothelial cells consist of 2 cell types in the alveolar region: general capillary cells (CAP1 or gCAPs) and aerocytes (CAP2 or aCAPs) [63]. Therefore, we used flow cytometry with CD117, CD31 and CD45
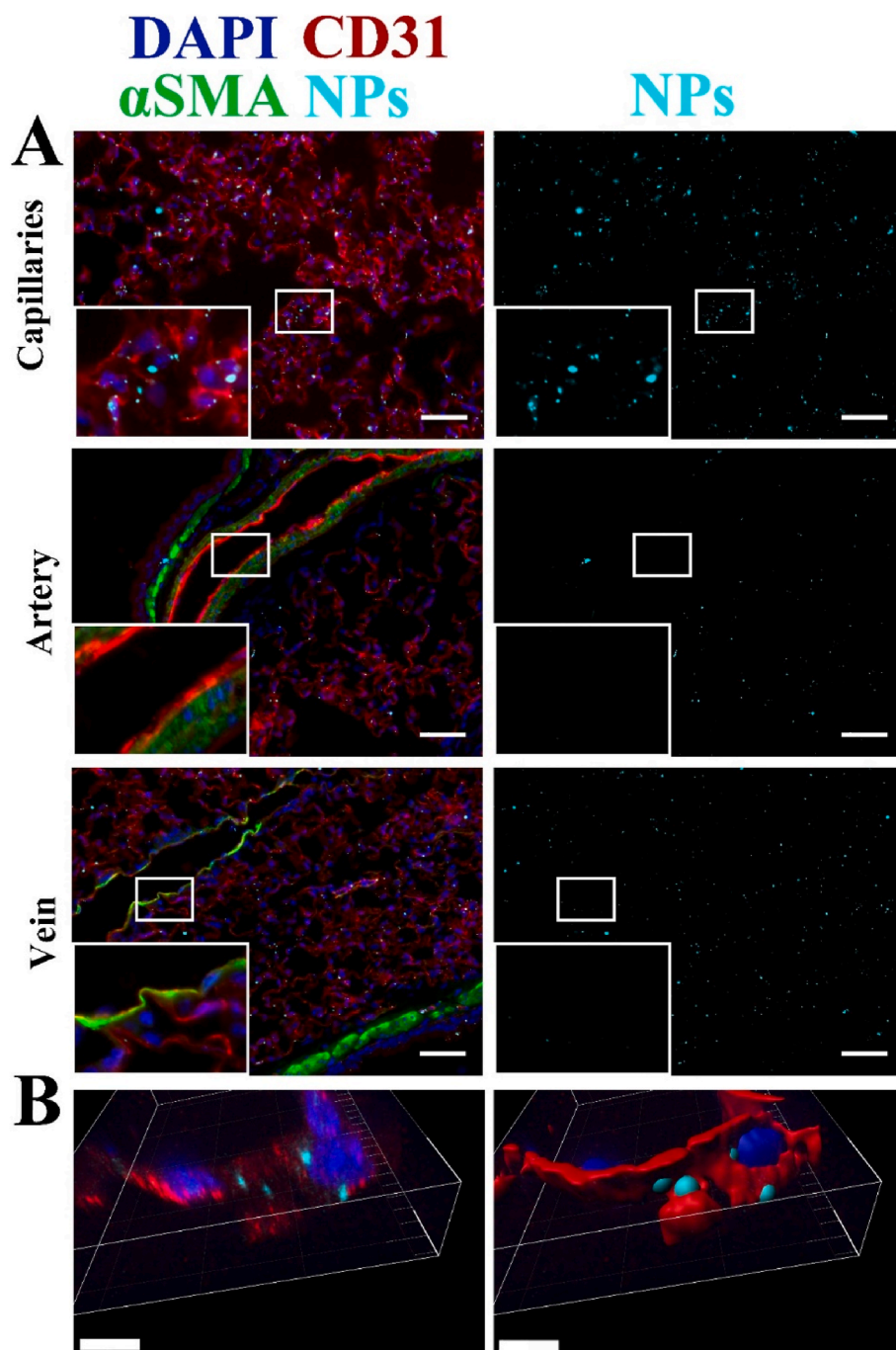
Fig. 5. Immunofluorescence of frozen lung sections after I.V. injection of DyLight 650-labeled P22–F1 nanoparticles (A) The nanoparticles (light blue) are observed in lung regions stained for endothelial marker CD31 (red) and smooth muscle cell marker αSMA (green). Cell nuclei were counterstained with DAPI (dark blue). (B) The cell surface 3D reconstruction of high magnification confocal images shows the nanoparticle fluorescence in capillary endothelial cells with subcellular and surface localizations. Scale bars: (A) 50 μm; (B) 6 μm.

antibodies to distinguish between CAP1 and CAP2 (Fig. 6A) [64]. Both CAP1 and CAP2 capillary endothelial cells were targeted by the P22–F1 PBAE nanoparticles with high efficiency (Fig. 6B). However, CAP2 cells had higher MFI (Fig. 6C–E), consistent with higher transfection rate due to larger cell surface area in CAP2 compared to CAP1 cells [63]. Thus, the P22–F1 PBAE nanoparticles accumulate in both CAP1 and CAP2 lung capillary endothelial cells without targeting the endothelium of other organs, arteries, and veins.

3.3. The P22–F1 PBAE nanoparticles are not toxic

Since biosafety is one of the most important considerations for nanoparticle delivery systems in biomedical and clinical applications, we evaluated the safety profile of the P22–F1 PBAE nanoparticles by measuring multiple clinical chemistry and hematology parameters in the peripheral blood of nanoparticle-injected mice.

After treatment with P22–F1 PBAE nanoparticles, mice had normal levels of alkaline phosphatase (ALP), aspartate transaminase (AST), Alanine aminotransferase (ALT) and Lactate dehydrogenase (LDH) (Fig. 7A and Table 1). Compared to vehicle-treated mice, there were no differences in concentrations of total protein, albumin, BUN, creatinine, and other clinical chemistry parameters. ALT, ALP AST, LDH, bilirubin, albumin, and total protein are usually related to the liver function. Lack of abnormalities in these parameters indicate normal liver function and the lack of liver toxicity. Although ALT value was slightly increased after the nanoparticle injection compared to the control group (Table 1), the value was within the normal range. The creatinine test is typically used as a measure of the kidney function, and no significant increase of creatinine was found in the P22–F1 PBAE nanoparticle-treated group. These results demonstrated that the P22–F1 PBAE nanoparticles are nontoxic to the liver and kidney after a single intravenous administration in mice.

In the hematology tests, the nanoparticle-treated group had no changes in the levels of hematologic parameters compared to the control group (Fig. 6B and Table 2). Measurements of white blood cells, red blood cells, and platelets in the peripheral blood used to diagnose inflammation, clotting disorders, and other blood diseases, remained within normal ranges after P22–F1 PBAE nanoparticle treatment, showing the benign nature of the nanoparticles. Thus, the PBAE nanoparticles did not alter the composition and viscosity of the peripheral blood. Furthermore, the body weight changes in mice were monitored for 5 days after the treatment. There were no body weight changes after the P22–F1 PBAE nanoparticle injection compared to the control group (Fig. 7C). Altogether, the fluorinated PBAE nanoparticles (P22–F1) did not exhibit toxicity as demonstrated by multiple clinical chemistry and hematology parameters and the lack of changes in the body weights.

3.4. The whole-body analysis of the P22–F1 PBAE nanoparticle efficiency and biodistribution

The P22–F1 PBAE nanoparticles were used for the *in vivo* biodistribution studies, in which the Luciferase reporter plasmid (gWiz-Luc) was encapsulated into the nanoparticles (NP) and injected intravenously to adult mice at a dose of 20 μg DNA per mouse at different NP/DNA mass ratios. Twenty-four hours after the injection, different organs were dissected and examined for bioluminescence. At NP/DNA ratios of 5:1 and 10:1, low luciferase expression was mostly observed in the spleen (Fig. 8A). At higher NP/DNA ratios, luciferase expression in the lung tissue was dramatically increased, while the luciferase expression in the spleen remained low (Fig. 8A). The highest luciferase expression in the lung tissue was reached at NP/DNA mass ratio of 40:1 and 50:1 (Fig. 8A–B). Luciferase expression in the liver, kidney, and heart was undetectable (Fig. 8A–B). Thus, the biodistribution and targeting efficiency of P22–F1 PBAE nanoparticles were found to be highly dependent on the NP/DNA ratio; the NP/DNA ratios of 40:1 and 50:1 resulted in the most effective lung-specific delivery. To further confirm lung-specific

delivery, the *in vivo* bioluminescence imaging (IVIS) and the micro-CT imaging of nanoparticle-treated mice were performed, demonstrating specific delivery of P22–F1 PBAE nanoparticles to the lung tissue *in vivo* (Fig. 8C–D). Low luciferase expression in the spleen was only detected by IVIS but not by micro-CT (Fig. 8C–D). At NP/DNA ratios of 40:1 and 50:1, luciferase activities in the lung were >10-fold higher than in spleen. (Fig. 8B).

Flow cytometry was used to investigate the influence of the NP/DNA ratio on the specificity of the P22–F1 PBAE nanoparticles in the lung tissue. Increasing the NP/DNA ratio had no effect on cell specificity; The nanoparticles were mainly found in lung endothelial cells, while they did not efficiently target fibroblasts, epithelial, hematopoietic, and lineage-negative cells, the latter of which contain pericytes, smooth muscle and other respiratory cell types (Fig. S14). These results demonstrate that the P22–F1 PBAE nanoparticles can deliver functional DNA (luciferase reporter) to endothelial cells in the lung tissue at high NP/DNA ratios.

Next, we investigated whether the P22–F1 PBAE nanoparticles can target endothelial cells in other organs. The mCherry minicircle DNA reporter plasmid was encapsulated into the P22–F1 PBAE nanoparticles at NP/DNA ratio of 50:1 and delivered intravenously. mCherry transfection efficiency in the lung endothelium was significantly higher compared to the endothelial cells isolated from the spleen (Fig. 8E–F). mCherry expression in endothelial cells of the heart, liver, and kidney was undetectable (Fig. 8E–F). Interestingly, the mCherry reporter was only detected in lung endothelial cells, whereas DyLight-650 labeled nanoparticles were present in endothelial cells of other organs (Figs. S15–S17). Thus, while the P22–F1 PBAE nanoparticles entered (or attached to) endothelial cells of many organs, the plasmid functional activity was only detected in lung endothelial cells. Altogether, the *in vivo* mCherry transfection flow cytometry analysis showed that the P22–F1 PBAE nanoparticles efficiently transfected lung microvascular endothelial cells without targeting endothelial cells of other organs, a finding consistent with IVIS whole-body imaging and micro-CT.

3.5. The fluorination is required to maintain the size and charge of the P22–F1 PBAE nanoparticles for lung endothelial-specific targeting

To investigate the factors that influence the *in vivo* transfection efficiency and biodistribution of the P22–F1 PBAE nanoparticles, the nanoparticles with four different formulations (P1, P21. P22, and P22–F1) were selected to perform DLS analysis and the *in vivo* distribution imaging. For the nanoparticles with only one amine (A2) in the backbone (P1), the hydrodynamic diameter of the nanoparticles did not change when the NP/DNA ratio was increasing (Fig. 9A). However, for the nanoparticles with two amines (A1 and A2), the size of the nanoparticles was decreased after increasing the NP/DNA ratio (Fig. 9). It is possible that the terpolymer chains have higher flexibility, making the size of the nanoparticles more controllable during the self-assemble. Compared to nanoparticles without fluorination (P21 and P22), the fluorinated PBAE nanoparticles (P22–F1) exhibit a much smaller hydrodynamic diameter at the low NP/DNA ratio, indicating that fluorination stabilizes the polymers chains in the nanoparticle complexes. Even at high NP/DNA ratios, the fluorinated PBAE nanoparticles exhibited a smaller size compared to the nanoparticles without fluorination (Fig. 9A). Measurement of zeta potentials showed that P21, P22, and P22–F1 nanoparticles have lower zeta potentials compared to the P1 formulation. However, zeta potentials for P21, P22, and P22–F1 were similar at high NP/DNA ratios (Fig. 9B). The bioluminescence whole-body imaging showed that the *in vivo* transfection efficiency and biodistribution are highly dependent on the formulations of PBAE polymers. Compared to the terpolymers, the transfection only occurred in the spleen for P1 nanoparticles (Fig. 9C–D). Bioluminescence distributions for the nanoparticles assembled by the terpolymers in the absence or presence of PEG (P21 vs P22) were similar and observed in both the lung and spleen (Fig. 9C–D). Fluorination of P22 nanoparticles (P22–F1)
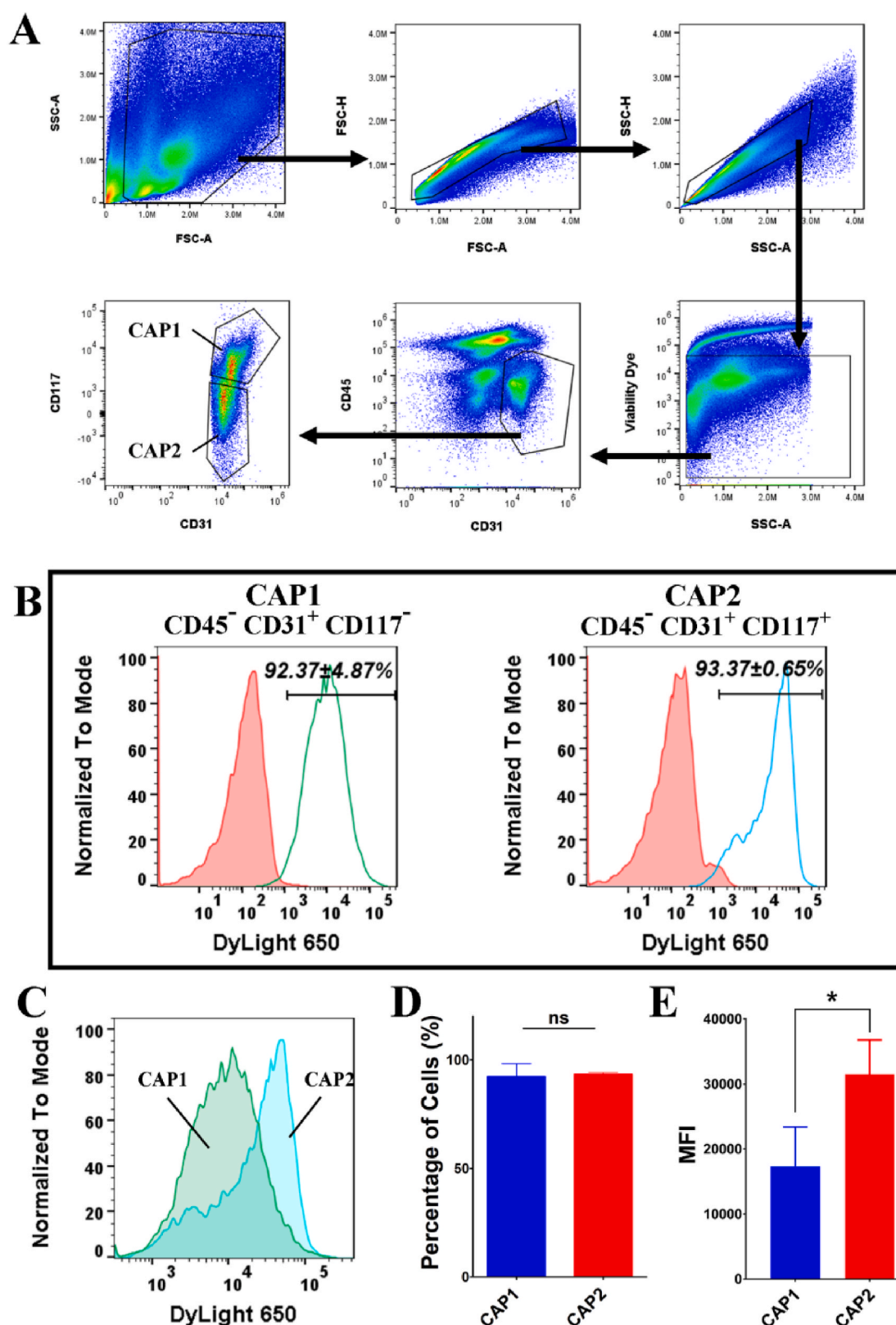
Fig. 6. Flow cytometry analysis of nanoparticle targeting of CAP1 and CAP2 lung capillary endothelial cells. (A) Gating strategy to identify CAP1 and CAP2 lung capillary endothelial cells. (B) Histogram analysis of the P22–F1 PBAE nanoparticle targeting of CAP1 and CAP2 endothelial cells (green curve) compared to the uninjected control (red curve). (C) Comparison of DyLight 650 fluorescence intensity using histograms cell uptake of the P22–F1 PBAE nanoparticles compared in CAP1 (green curve) and CAP2 (blue curve) lung capillary endothelial cells. (D) Juxtaposition of the targeting efficiency as percentages of cells targeted by the nanoparticles. (E) Juxtaposition of MFI in CAP1 and CAP2 cells.
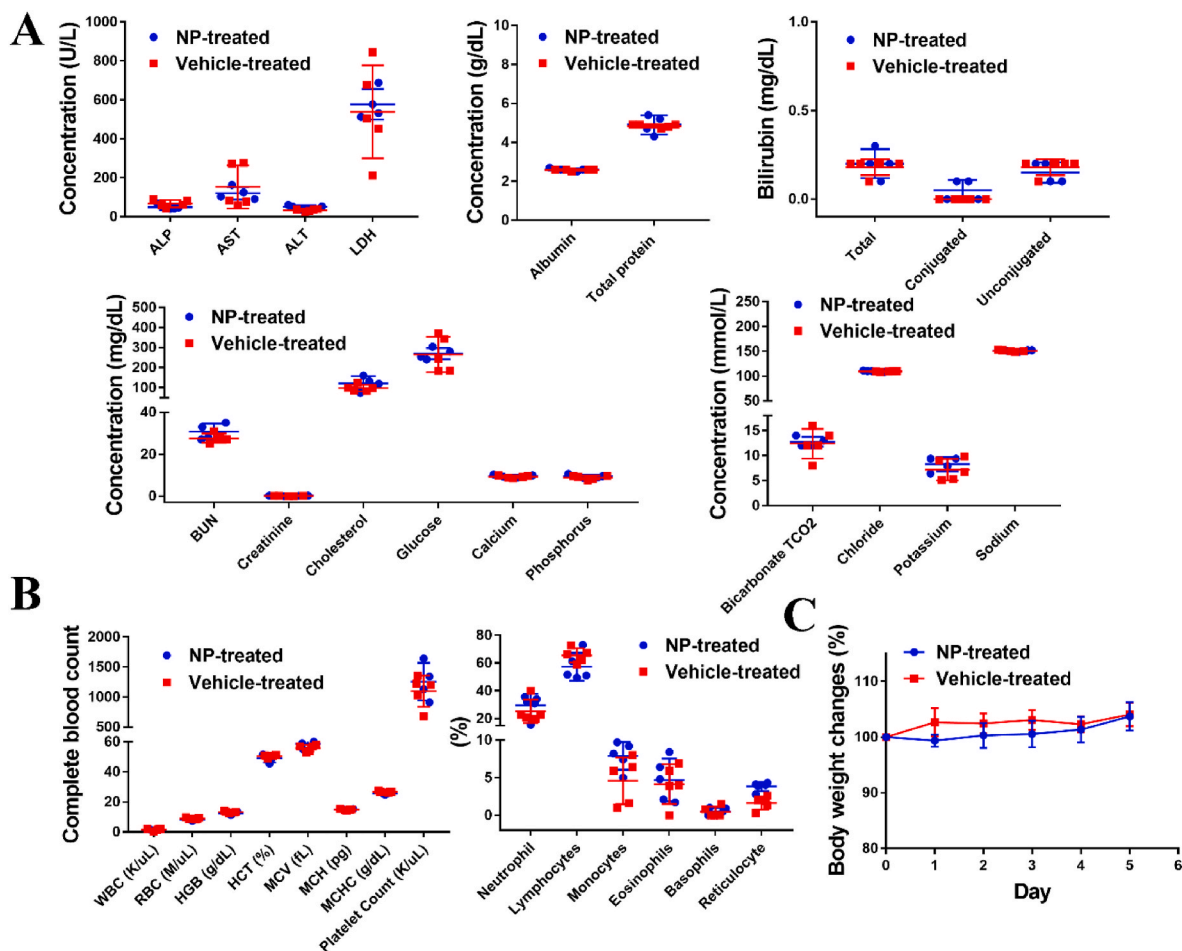
Fig. 7. Toxicity studies of the P22–F1 PBAE nanoparticles. The peripheral blood was collected from mice 5 days after a single intravenous injection of the P22–F1 PBAE nanoparticles. (A) The peripheral blood was assayed for major parameters in clinical chemistry, including those related to the liver and kidney metabolic panels, n = 5 mice per group. (B) Major parameters in hematology after analysis of peripheral blood. (C) Body weight changes after nanoparticle treatment.

Table 1
Clinical chemistry of the treated and control mice (n = 5 mice per group, * is $P < 0.05$, ns is not significant).

|	Control	Nanoparticle	P Value	Significance	Normal Range
ALP (U/L)	64.25 ± 16.94	49.25 ± 11.12	0.122647	ns	29–78
AST (U/L)	124.25 ± 88.66	121 ± 27.63	0.555211	ns	47–182
ALT(U/L)	32.5 ± 5.67	50 ± 8.45	0.037089	*	18–71
LDH(U/L)	461.5 ± 166.33	577.5 ± 67.89	0.743843	ns	159–1045
Albumin (g/dL)	2.575 ± 0.04	2.6 ± 0.07	0.680639	ns	2.6–3.7
Total protein (g/dL)	4.825 ± 0.08	4.9 ± 0.43	0.826118	ns	4.7–6.6
Total Bilirubin (mg/dL)	0.175 ± 0.04	0.2 ± 0.07	0.680639	ns	0.1–0.4
Bilirubin - Conjugated (mg/dL)	0 ± 0	0.05 ± 0.05	0.18169	ns	–
Bilirubin - Unconjugated (mg/dL)	0.175 ± 0.04	0.15 ± 0.05	0.427976	ns	–
BUN (mg/dL)	27.75 ± 2.16	30.75 ± 3.341	0.211502	ns	18–29
Creatinine (mg/dL)	0.05 ± 0.05	0.125 ± 0.08	0.285882	ns	0.0–0.4
Cholesterol (mg/dL)	100.75 ± 14.77	121.25 ± 31.04	0.288916	ns	85–275
Glucose	238.5 ± 65.19	269.75 ± 24.25	0.917859	ns	137–361
Calcium	9.025 ± 0.44	9.575 ± 0.574	0.378196	ns	9.9–12.4
Phosphorus	8.75 ± 0.93	9.425 ± 0.73	0.365724	ns	7.9–14.1
Bicarbonate TCO2	12.5 ± 2.96	12.75 ± 0.82	0.813887	ns	–
Chloride	109.5 ± 0.5	109.75 ± 1.08	0.486109	ns	106.1–130.7
Potassium	6.525 ± 1.55	8.275 ± 1.24	0.390683	ns	7.84–14.18
Sodium	151 ± 1.58	151 ± 1.22	0.850152	ns	137.7–155.2

significantly improved bioluminescence in the lung tissue but decreased luciferase activity in the spleen (Fig. 9C–D). Thus, fluorination is required for P22–F1 nanoparticle-mediated delivery of functional DNA plasmid to lung microvascular endothelial cells *in vivo*.

4. Discussion

In this study, we designed a fluorinated PBAE nanoparticle formulation capable of targeting pulmonary microvascular endothelium with high transfection efficiency and organ specificity. Our initial studies

Table 2
Hematology of the treated and control mice (n = 5 mice per group, ns is not significant).

	Control	Nanoparticle	P Value	Significance	Normal Range
CBC Parameters					
WBC (K/uL)	1.375 ± 0.67	1.6 ± 0.36	0.805459	ns	4.44–16.21
RBC (M/uL)	8.97 ± 0.414	8.3 ± 0.66	0.165662	ns	7.31–12.27
HGB (g/dL)	13.45 ± 0.43	12.64 ± 0.84	0.235666	ns	11.2–18.4
HCT (%)	50.25 ± 0.9	49.58 ± 2.43	0.411704	ns	38.2–74.7
MCV (fL)	56.25 ± 1.92	59 ± 2.27	0.122252	ns	46.5–69.0
MCH (pg)	15 ± 0.25	15.06 ± 0.3	0.59824	ns	12.9–18.1
MCHC (g/dL)	26.75 ± 0.52	25.48 ± 0.62	0.033013	*	21.3–33.5
Platelet Count (K/uL)	1067.25 ± 249.86	1389.8 ± 269.42	0.217499	ns	469–2374
Percentage of cells					
Neutrophil (%)	25.875 ± 8.23	25.28 ± 8.23	0.428227	ns	7.3–55.68
Band (%)	none seen	none seen			–
Lymphocytes (%)	65.54 ± 4.87	59.275 ± 9.01	0.154666	ns	37.50–86.46
Monocytes (%)	4.58 ± 2.92	7.575 ± 1.70	0.081691	ns	0–13.44
Eosinophils (%)	4.14 ± 2.14	4.25 ± 2.67	0.763759	ns	0.18–6.64
Basophils (%)	0.46 ± 0.34	0.375 ± 0.41	0.95838	ns	0.00–0.38
Metamyelocyte (%)	none seen	none seen			–
Myelocyte (%)	none seen	none seen			–
Promyelocyte (%)	none seen	none seen			–
Unclassified (%)	none seen	none seen			–
RBC Morphology	Normal	Normal			–
Reticulocyte (%)	2.54 ± 0.17	3.8 ± 0.58	0.006176	**	1.0–6.0
Absolute Reticulocyte (K/uL)	226.5 ± 22.87	308 ± 57.99	0.031393	*	–
Nucleated RBC (/100 WBC)	none seen	none seen			–
Polychromasia	Slight	Slight			–
Anisocytosis	Slight	Slight			–
Poikilocytosis	none seen	none seen			–
Heinz bodies	none seen	none seen			–
Absolutes					
Unclassified (/uL)	none seen	none seen			–
Neutrophil (/uL)	336.4 ± 126.38	523.75 ± 234.68	0.256969	ns	200–800
Band (/uL)	none seen	none seen			–
Lymphocyte (/uL)	1002.6 ± 467.45	999.75 ± 286.32	0.74305	ns	1000–3100
Monocyte (/uL)	76.6 ± 51.36	124.5 ± 27.52	0.179164	ns	0–1490
Eosinophil (/uL)	76 ± 53.59	71.75 ± 44.06	0.885977	ns	0–80
Basophil (/uL)	8 ± 12.24	5 ± 5	0.763757	ns	0–40
Metamyelocyte (/uL)	none seen	none seen			–
Myelocyte (/uL)	none seen	none seen			–
Promyelocyte (/uL)	none seen	none seen			–

focused on developing effective formulations for *in vitro* transfection and found that the alkyl chain amines in backbone synthesis can significantly enhance the transfection performance of the PBAE nanoparticles. The PBAE polymer synthesis was found to be sensitively controlled by the A1 to A2 ratio for optimum transfection efficiencies. It is likely that the underlying mechanism of the A1 to A2 ratio effects is related to the hydrophobicity of the monomers on the polymer backbones in order to form stable nanoparticles in gene delivery [65,66]. PEG has been widely used in nanoparticle synthesis to improve nanoparticle stability, increase circulation time *in vivo*, and reduce toxicity [53,67]. In this study, the addition of PEG at 3%–6% in the end caps was found to increase the transfection efficiency. However, further increasing the PEG ratio in end caps reduced transfection. Therefore, the best PEGylation ratio for this amphiphilic PBAE capping was controlled in the range of 3%–6%. Moreover, there was a large difference between the different fluorous ligands in terms of *in vitro* transfection efficiency. Based on our data, the transfection efficiency can only be increased by modification of Pentadecafluorooctanoyl chloride (F1) and by changing the fluorous ligand type. However, increasing the length of the fluorous ligands may have a negative influence on transfections. Unlike PEGylation, fluorination not only increased the percentage of transfected cells but also improved the strength of the transfection. These results support the hypothesis that fluorous ligands enable the PBAE nanoparticles to enter the cell more efficiently.

While the *in vivo* transfection is more complex, our data showed high endothelial targeting efficiency via the amphiphilic PBAE nanoparticles. We found that PEGylation increases both the targeting percentage and strength as it, likely, delays nanoparticle clearance in circulation before reaching pulmonary endothelium, while fluorination exerts a similar effect on the nanoparticles *in vivo*. The underlying mechanism for the nanoparticle targeting to microvascular endothelium was discussed in our previous studies [16,39], emphasizing that the efficiency of endothelial targeting is highly dependent on the size and surface charge of the nanoparticles due to interactions between the nanoparticles and the microvascular bed. The PBAE nanoparticles were primarily located in the lung microvasculature as supported by confocal microscopy and flow cytometry for CAP1 and CAP2 lung capillary endothelial cells. Moreover, the nanoparticle size and charge influence the bio-distribution of the nanoparticles and are dependent on NP/DNA ratio. Interestingly, *in vivo* luciferase imaging demonstrated that at low NP/DNA ratio of 10, the nanoparticles have a relatively large size (135.83 ± 2.41 nm), and the transfection occurs mainly in the spleen. With the increase of NP/DNA ratio to 50, the size of the nanoparticles was reduced (86.00 ± 0.32 nm) dramatically, changing bioluminescence distribution in which the lung becomes the major targeted organ. Additional isotope studies are needed to investigate pharmacokinetics and pharmacodynamics. However, our IVIS and Micro-CT results indicate that the nanoparticles are capable of delivering the report plasmids and transfecting the cells in the lung-specific manner. The transfection patterns and organ specificity of nanoparticles *in vivo* can be controlled by modifying the backbone structures of the nanoparticles, adjusting the contents of capping agents, and optimizing the polymer-to-nucleic acid ratio. Our results consistent with published studies demonstrated that the size of the nanoparticles is important for its *in vivo* fate because the liver and spleen can trap particles with larger sizes [68,69]. It was also found that larger nanoparticles (hydrodynamic size >100 nm) are prone
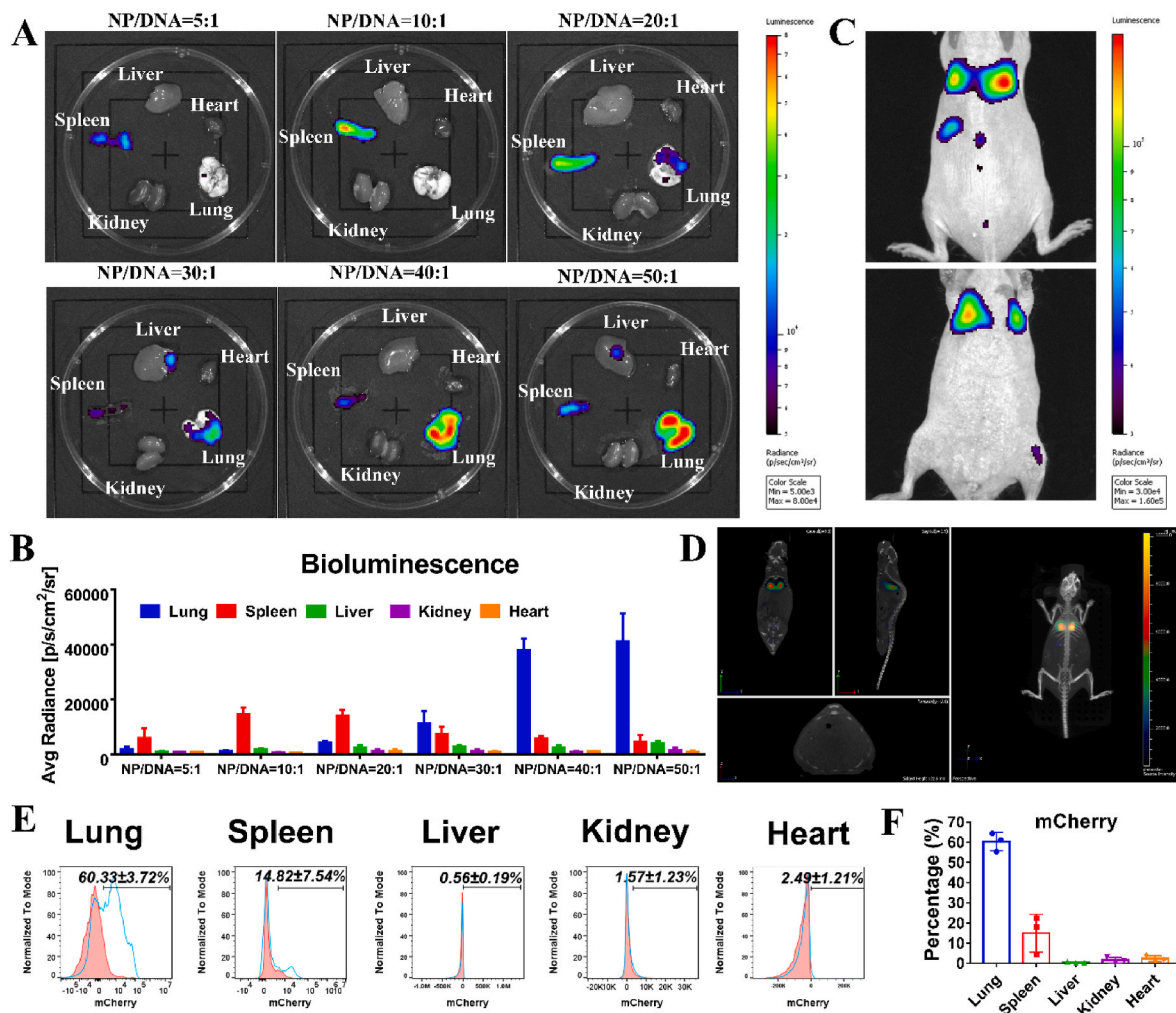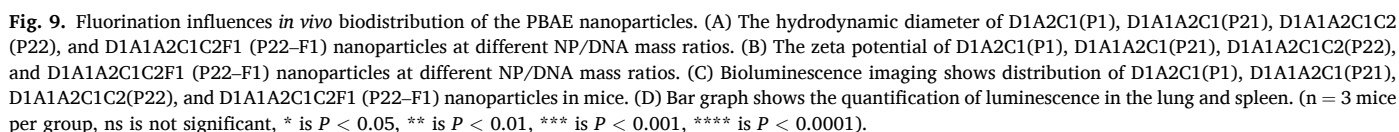
Fig. 8. *In vivo* transfection studies of P22–F1 PBAE nanoparticles. (A) Luminescent images show the biodistribution of luciferase expression at different nanoparticle to DNA ratios (10:1; 20:1; 30:1; 40:1, and 50:1) in dissected mouse organs. (B) Quantification of luminescence from different organs (n = 3 mice per group); (C) IVIS whole-body imaging shows the *in vivo* bioluminescence following treatment with P22–F1 PBAE nanoparticles. Ventral (top) and dorsal (bottom) view of the mouse are shown. (D) MicroCT images show the bioluminescence in the lung of mice treated with P22–F1 PBAE nanoparticles. (E) Flow cytometry shows mCherry reporter activity in endothelial cells isolated from different murine organs. Blue curve: P22–F1 PBAE nanoparticles; Red curve: untreated control. (F) The bar graph shows the mCherry transfection efficiency in endothelial cells from different organs (n = 3 mice per group).

to accumulate in spleen, liver, or be destroyed by the bone marrow [70, 71]. Compared to nanoparticle sizes, the changes in the surface charge were insignificant when increasing the NP/DNA ratio. Thus, it is possible that small sizes of the PBAE nanoparticles at high NP/DNA ratios can enhance the nanoparticles by avoiding the elimination through the spleen, leading to the accumulation of the nanoparticles in lungs via interaction between the nanoparticles and the microvascular bed. On the other hand, the fluorination of PBAE nanoparticles plays an important role in pulmonary transfection. However, there is no clear evidence to show that pulmonary endothelial cells contain any receptors for fluorous molecules. In previously reported studies, it was found that different types of fluorinated nanoparticles exhibited different tissue tropism [72–74]. It is widely recognized that the fluorination of nanoparticles can change the physicochemical properties of the nanoparticles, which further influences the way the nanoparticles interact with biological molecules like proteins and lipids [72,75,76]. In the context of lung tissue, it is important to note that endothelial cells are enveloped by glycocalyx, a crucial component that significantly contributes to blood vessel homeostasis and facilitates gas exchange [77]. As a carbohydrate-rich layer, glycocalyx contains numerous hydroxy groups that can interact with fluorine molecules on the nanoparticles via hydrogen bonds [78]. This specific property of fluorinated nanoparticles

may help to bind the surface of endothelial cells more efficiently. Furthermore, the fluorination of nanoparticles can improve gene delivery by increasing stability, decreasing toxicity, and enhancing cellular uptake and endosomal escape of the nanoparticles [79,80]. Therefore, fluorination increases both endothelial cell targeting and transfection efficiency. However, fluorination is not the sole factor that influences targeting efficiency. The surface charge of nanoparticles also plays an important role in endothelial cell targeting. Glycocalyx on the surface of endothelial cells is negatively charged [77]. Due to their positively charged surfaces, the P22–F1 nanoparticles exhibit an inherent attraction or affinity towards endothelial cells. Published studies have shown that nanoparticles with specific hydrodynamic diameters and charges exhibit improved efficiency in targeting pulmonary endothelial cells. This enhanced targeting capability may be attributed to the nanoparticles' capacity to enter and remain within the microvasculature [16, 39]. The lungs possess dense microvascular networks that facilitate the accumulation of specific nanoparticles, whereas the liver and spleen tend to retain a higher proportion of aggregates that do not enhance cell transfections. Therefore, the transfection is not from the large aggregates, but this specific nanoparticle formulation combined the fluorination, surface charge, and size for the optimal pulmonary transfection efficiency. Serum proteins also play important roles in nanoparticle

Fig. 9. Fluorination influences *in vivo* biodistribution of the PBAE nanoparticles. (A) The hydrodynamic diameter of D1A2C1(P1), D1A1A2C1(P21), D1A1A2C1C2 (P22), and D1A1A2C1C2F1 (P22–F1) nanoparticles at different NP/DNA mass ratios. (B) The zeta potential of D1A2C1(P1), D1A1A2C1(P21), D1A1A2C1C2(P22), and D1A1A2C1C2F1 (P22–F1) nanoparticles at different NP/DNA mass ratios. (C) Bioluminescence imaging shows distribution of D1A2C1(P1), D1A1A2C1(P21), D1A1A2C1C2(P22), and D1A1A2C1C2F1 (P22–F1) nanoparticles in mice. (D) Bar graph shows the quantification of luminescence in the lung and spleen. (n = 3 mice per group, ns is not significant, * is $P < 0.05$, ** is $P < 0.01$, *** is $P < 0.001$, **** is $P < 0.0001$).

stability and targeting. Nanoparticle surfaces can absorb serum proteins in physiological media and form "Protein corona". Previous studies showed that the protein corona can shield the small targeting moieties, which may cause the ligands-mediate-targeting ability loss [81,82]. However, in surface charge-based passive targeting, the positively charged nanoparticles can keep strong electrostatic interactions with negatively charged surfaces even if the nanoparticle surface is covered by protein corona [11,83]. Thus, P22–F1 can keep a high targeting and transfection efficiency in the presence of serum *in vivo*. Current results showed that the P22–F1 nanoparticles exhibit high pulmonary endothelial cell targeting and transfection efficiency. However, additional studies are needed to better understand the interaction of the nanoparticles with blood cells and serum proteins in the circulation. It is also unclear whether the P22–F1 nanoparticles can maintain their lung endothelial-specific properties after administration through intra-tracheal and oral routes. Given the lack of obvious toxicity, the P22–F1 nanoparticles hold promise for future clinical applications as lung-specific delivery vehicles in pulmonary vascular disorders.

5. Conclusion

In conclusion, we have developed a facile synthesis of amphiphilic PBAE nanoparticles for pulmonary endothelial specific targeting and effective delivery. The transfection efficiency of PBAE nanoparticles can be optimized by changing the ratio of two alkyl chains in the backbones. The addition of PEG in the end cap and suitable fluorination can further increase the transfection efficiency. Based on flow cytometry and confocal imaging, the PBAE nanoparticles were mainly taken up by lung microvascular endothelial cells. The optimized formulation with PEG and fluorous ligand modifications increased the endothelial targeting efficiency to above 90%. Based on IVIS whole body imaging and microCT, at low NP/DNA ratios, the transfection occurred only in the spleen, but the lung became the primary targeted organ after increasing the NP/DNA ratio. Clinical chemistry and hematology of the peripheral blood showed that the PBAE nanoparticles are nontoxic in experimental mice. The present study shows that these specifically designed PBAE nanoparticles have promise for developing new therapies to correct

endothelial dysfunctions in pulmonary vascular diseases.

Ethics approval

The study protocol and experimental procedures involving animal subjects were reviewed and approved by Cincinnati Children's Research Foundation Institutional Animal Care and Use Committee. Appropriate measures were taken to minimize any potential suffering or harm, following the ethical guidelines for animal research.

CRediT authorship contribution statement

Zicheng Deng: Conceptualization, Methodology, Formal analysis, Investigation, Data curation, Writing – original draft. **Wen Gao:** Methodology, Investigation, Data curation. **Fatemeh Kohram:** Methodology, Investigation. **Enhong Li:** Methodology. **Tanya V. Kalin:** Methodology, Validation, Investigation, Resources. **Donglu Shi:** Conceptualization, Methodology, Validation, Formal analysis, Investigation, Writing – original draft. **Vladimir V. Kalinichenko:** Conceptualization, Methodology, Validation, Formal analysis, Investigation, Resources, Project administration, Writing – original draft, Funding acquisition.

Declaration of competing interest

The authors declare no conflict of interest.

Acknowledgement

Appendix A. Supplementary data

Supplementary data to this article can be found online at https://doi.org/10.1016/j.bioactmat.2023.07.022.

References

[1] Y. Cai, C. Bolte, T. Le, C. Goda, Y. Xu, T.V. Kalin, V.V. Kalinichenko, FOXF1 maintains endothelial barrier function and prevents edema after lung injury, Sci. Signal. 9 (2016), https://doi.org/10.1126/scisignal.aad1899 ra40–ra40.

[2] A. Pradhan, A. Dunn, V. Ustiyan, C. Bolte, G. Wang, J.A. Whitsett, Y. Zhang, A. Porollo, Y.-C. Hu, R. Xiao, P. Szafranski, D. Shi, P. Stankiewicz, T.V. Kalin, V. V. Kalinichenko, The S52F FOXF1 mutation inhibits STAT3 signaling and causes alveolar capillary dysplasia, Am. J. Respir. Crit. Care Med. 200 (2019) 1045–1056, https://doi.org/10.1164/rccm.201810-1897OC.

[3] C. Bolte, V. Ustiyan, X. Ren, A.W. Dunn, A. Pradhan, G. Wang, O.A. Kolesnichenko, Z. Deng, Y. Zhang, D. Shi, J.M. Greenberg, A.H. Jobe, T.V. Kalin, V. V. Kalinichenko, Nanoparticle delivery of proangiogenic transcription factors into the neonatal circulation inhibits alveolar simplification caused by hyperoxia, Am. J. Respir. Crit. Care Med. 202 (2020) 100–111, https://doi.org/10.1164/rccm.201906-1232OC.

[4] F. Sun, G. Wang, A. Pradhan, K. Xu, J. Gomez-Arroyo, Y. Zhang, G.T. Kalin, Z. Deng, R.J. Vagnozzi, H. He, A.W. Dunn, Y. Wang, A.J. York, R.S. Hegde, J. C. Woods, T V Kalin, J.D. Molkentin, V V Kalinichenko, Nanoparticle delivery of STAT3 alleviates pulmonary hypertension in a mouse model of alveolar capillary dysplasia, Circulation 144 (2021) 539–555, https://doi.org/10.1161/CIRCULATIONAHA.121.053980.

[5] C. Bolte, J.A. Whitsett, T.V. Kalin, V.V. Kalinichenko, Transcription factors regulating embryonic development of pulmonary vasculature, Adv. Anat. Embryol. Cell Biol. 228 (2018) 1–20, https://doi.org/10.1007/978-3-319-68483-3_1.

[6] L. Wang, C. Xiao, Y. Liang, Z. Weng, W. Yang, Research advances in COPD drugs and novel targets, Nano Life 11 (2021), 2140008, https://doi.org/10.1142/s1793984421400080.

[7] H. Yin, R.L. Kanasty, A.A. Eltoukhy, A.J. Vegas, J.R. Dorkin, D.G. Anderson, Non-viral vectors for gene-based therapy, Nat. Rev. Genet. 15 (2014) 541–555, https://doi.org/10.1038/nrg3763.

[8] T V Mashel, Y V Tarakanchikova, A.R. Muslimov, M. V Zyuzin, A.S. Timin, K. V Lepik, B. Fehse, Overcoming the delivery problem for therapeutic genome editing: current status and perspective of non-viral methods, Biomaterials 258 (2020), 120282, https://doi.org/10.1016/j.biomaterials.2020.120282.

[9] Gao Patil, Li Lin, Tian Dang, Jiang Zhang, Qian Qadir, The development of functional non-viral vectors for gene delivery, Int. J. Mol. Sci. 20 (2019) 5491, https://doi.org/10.3390/ijms20215491.

[10] E. Warga, B. Austin-Carter, N. Comolli, J. Elmer, Nonviral vehicles for gene delivery, Nano Life 11 (2021), 2130002, https://doi.org/10.1142/S1793984421300028.

[11] Z. Deng, S. Wu, Y. Wang, D. Shi, Circulating tumor cell isolation for cancer diagnosis and prognosis, EBioMedicine 83 (2022), 104237, https://doi.org/10.1016/j.ebiom.2022.104237.

[12] S. Sun, Y. Wang, R. Zhou, Z. Deng, Y. Han, X. Han, W. Tao, Z. Yang, C. Shi, D. Hong, J. Li, D. Shi, Z. Zhang, Targeting and regulating of an oncogene via nanovector delivery of MicroRNA using patient-derived tumor xenografts, Theranostics 7 (2017) 677–693, https://doi.org/10.7150/thno.16357.

[13] A. Alu, L. Chen, H. Lei, Y. Wei, X. Tian, X. Wei, Intranasal COVID-19 vaccines: from bench to bed, EBioMedicine 76 (2022), 103841, https://doi.org/10.1016/j.ebiom.2022.103841.

[14] X. Han, Z. Deng, Z. Yang, Y. Wang, H. Zhu, B. Chen, Z. Cui, R.C. Ewing, D. Shi, Biomarkerless targeting and photothermal cancer cell killing by surface-electrically-charged superparamagnetic Fe 3 O 4 composite nanoparticles, Nanoscale 9 (2017) 1457–1465, https://doi.org/10.1039/C6NR07161A.

[15] Z. Deng, J. Lin, S.L. Bud'ko, B. Webster, T. V Kalin, V. V Kalinichenko, D. Shi, Dual targeting with cell surface electrical charge and folic acid via superparamagnetic Fe3O4@Cu2−xS for photothermal cancer cell killing, Cancers 13 (2021) 5275, https://doi.org/10.3390/cancers13215275.

[16] Z. Deng, G.T. Kalin, D. Shi, V.V. Kalinichenko, Nanoparticle delivery systems with cell-specific targeting for pulmonary diseases, Am. J. Respir. Cell Mol. Biol. 64 (2021) 292–307, https://doi.org/10.1165/rcmb.2020-0306TR.

[17] S. Danilov, E. Atochina, H. Hiemisch, T. Churak-ova, A. Moldobaeva, I. Sakharov, G. Deichman, U. Ryan, V.R. Muzykantov, Interaction of mAb to angiotensin-converting enzyme (ACE) with antigen in vitro and in vivo: antibody targeting to the lung induces ACE antigenic modulation, Int. Immunol. 6 (1994) 1153–1160, https://doi.org/10.1093/intimm/6.8.1153.

[18] V.V. Shuvaev, M. Khoshnejad, K.W. Pulsipher, R.Y. Kiseleva, E. Arguiri, J. C. Cheung-Lau, K.M. LeFort, M. Christofidou-Solomidou, R.V. Stan, I. J. Dmochowski, V.R. Muzykantov, Spatially controlled assembly of affinity ligand and enzyme cargo enables targeting ferritin nanocarriers to caveolae, Biomaterials 185 (2018) 348–359, https://doi.org/10.1016/j.biomaterials.2018.09.015.

[19] C.F. Greineder, J.B. Brenza, R. Carnemolla, S. Zaitsev, E.D. Hood, D.C. Pan, B.-S. Ding, C.T. Esmon, A.M. Chacko, V.R. Muzykantov, Dual targeting of therapeutics to endothelial cells: collaborative enhancement of delivery and effect, FASEB J 29 (2015) 3483–3492, https://doi.org/10.1096/fj.15-271213.

[20] C.F. Greineder, A.-M. Chacko, S. Zaytsev, B.J. Zern, R. Carnemolla, E.D. Hood, J. Han, B.-S. Ding, C.T. Esmon, V.R. Muzykantov, Vascular immunotargeting to endothelial determinant ICAM-1 enables optimal partnering of recombinant scFv-thrombomodulin fusion with endogenous cofactor, PLoS One 8 (2013), e80110.

[21] P.N. Reynolds, S.A. Nicklin, L. Kaliberova, B.G. Boatman, W.E. Grizzle, I. V Balyasnikova, A.H. Baker, S.M. Danilov, D.T. Curiel, Combined transductional and transcriptional targeting improves the specificity of transgene expression in vivo, Nat. Biotechnol. 19 (2001) 838–842, https://doi.org/10.1038/nbt0901-838.

[22] A.M. Reynolds, M.D. Holmes, S.M. Danilov, P.N. Reynolds, Targeted gene delivery of BMPR2 attenuates pulmonary hypertension, Eur. Respir. J. 39 (2012) 329–343, https://doi.org/10.1183/09031936.00187310.

[23] I. Morecroft, K. White, P. Caruso, M. Nilsen, L. Loughlin, R. Alba, P.N. Reynolds, S. M. Danilov, A.H. Baker, M.R. MacLean, Gene therapy by targeted adenovirus-mediated knockdown of pulmonary endothelial Tph1 attenuates hypoxia-induced pulmonary hypertension, Mol. Ther. 20 (2012) 1516–1528, https://doi.org/10.1038/mt.2012.70.

[24] E.N. Atochina, H.H. Hiemisch, V.R. Muzykantov, S.M. Danilov, Systemic administration of platelet-activating factor in rat reduces specific pulmonary uptake of circulating monoclonal antibody to angiotensin-converting enzyme, Lung 170 (1992) 349–358, https://doi.org/10.1007/BF00177581.

[25] H. Parhiz, V V Shuvaev, N. Pardi, M. Khoshnejad, R.Y. Kiseleva, J.S. Brenner, T. Uhler, S. Tuyishime, B.L. Mui, Y.K. Tam, T.D. Madden, M.J. Hope, D. Weissman, V.R. Muzykantov, PECAM-1 directed re-targeting of exogenous mRNA providing two orders of magnitude enhancement of vascular delivery and expression in lungs independent of apolipoprotein E-mediated uptake, J. Contr. Release 291 (2018) 106–115, https://doi.org/10.1016/j.jconrel.2018.10.015.

[26] E.A. Simone, B.J. Zern, A.-M. Chacko, J.L. Mikitsh, E.R. Blankemeyer, S. Muro, R. V Stan, V.R. Muzykantov, Endothelial targeting of polymeric nanoparticles stably labeled with the PET imaging radioisotope iodine-124, Biomaterials 33 (2012) 5406–5413, https://doi.org/10.1016/j.biomaterials.2012.04.036.

[27] P.M. Glassman, J.W. Myerson, L.T. Ferguson, R.Y. Kiseleva, V V Shuvaev, J. S. Brenner, V.R. Muzykantov, Targeting drug delivery in the vascular system: focus on endothelium, Adv. Drug Deliv. Rev. 157 (2020) 96–117, https://doi.org/10.1016/j.addr.2020.06.013.

[28] B.J. Zern, A.-M. Chacko, J. Liu, C.F. Greineder, E.R. Blankemeyer, R. Radhakrishnan, V. Muzykantov, Reduction of nanoparticle avidity enhances the selectivity of vascular targeting and PET detection of pulmonary inflammation, ACS Nano 7 (2013) 2461–2469, https://doi.org/10.1021/nn305773f.

[29] R.Y. Kiseleva, P.G. Glassman, K.M. LeForte, L.R. Walsh, C.H. Villa, V V Shuvaev, J. W. Myerson, P.A. Aprelev, O.A. Marcos-Contreras, V.R. Muzykantov, C. F. Greineder, Bivalent engagement of endothelial surface antigens is critical to prolonged surface targeting and protein delivery in vivo, FASEB J 34 (2020) 11577–11593, https://doi.org/10.1096/fj.201902515RR.

[30] C. Garnacho, S.M. Albelda, V.R. Muzykantov, S. Muro, Differential intra-endothelial delivery of polymer nanocarriers targeted to distinct PECAM-1 epitopes, J. Contr. Release 130 (2008) 226–233, https://doi.org/10.1016/j.jconrel.2008.06.007.

[31] S. Muro, C. Gajewski, M. Koval, V.R. Muzykantov, ICAM-1 recycling in endothelial cells: a novel pathway for sustained intracellular delivery and prolonged effects of drugs, Blood 105 (2005) 650–658, https://doi.org/10.1182/blood-2004-05-1714.

[32] J.W. Myerson, O. McPherson, K.G. DeFrates, J.H. Towslee, O.A. Marcos-Contreras, V. V Shuvaev, B. Braender, R.J. Composto, V.R. Muzykantov, D.M. Eckmann, Cross-linker-Modulated nanogel flexibility correlates with tunable targeting to a sterically impeded endothelial marker, ACS Nano 13 (2019) 11409–11421, https://doi.org/10.1021/acsnano.9b04789.

[33] J.W. Myerson, B. Braender, O. Mcpherson, P.M. Glassman, R.Y. Kiseleva, V. V Shuvaev, O. Marcos-Contreras, M.E. Grady, H.-S. Lee, C.F. Greineder, R. V Stan, R. J. Composto, D.M. Eckmann, V.R. Muzykantov, Flexible nanoparticles reach sterically obscured endothelial targets inaccessible to rigid nanoparticles, Adv. Mater. 30 (2018), 1802373, https://doi.org/10.1002/adma.201802373.

[34] J. Han, V.V. Shuvaev, P.F. Davies, D.M. Eckmann, S. Muro, V.R. Muzykantov, Flow shear stress differentially regulates endothelial uptake of nanocarriers targeted to distinct epitopes of PECAM-1, J. Contr. Release 210 (2015) 39–47, https://doi.org/10.1016/j.jconrel.2015.05.006.

[35] V. V Shuvaev, S. Muro, E. Arguiri, M. Khoshnejad, S. Tliba, M. Christofidou-Solomidou, V.R. Muzykantov, Size and targeting to PECAM vs ICAM control endothelial delivery, internalization and protective effect of multimolecular SOD conjugates, J. Contr. Release 234 (2016) 115–123, https://doi.org/10.1016/j.jconrel.2016.05.040.

[36] M. Khoshnejad, C.F. Greineder, K.W. Pulsipher, C.H. Villa, B. Altun, D.C. Pan, A. Tsourkas, I.J. Dmochowski, V.R. Muzykantov, Ferritin nanocages with biologically orthogonal conjugation for vascular targeting and imaging, Bioconjugate Chem. 29 (2018) 1209–1218, https://doi.org/10.1021/acs.bioconjchem.8b00004.

[37] A.C. Anselmo, S. Kumar, V. Gupta, A.M. Pearce, A. Ragusa, V. Muzykantov, S. Mitragotri, Exploiting shape, cellular-hitchhiking and antibodies to target nanoparticles to lung endothelium: synergy between physical, chemical and biological approaches, Biomaterials 68 (2015) 1–8, https://doi.org/10.1016/j.biomaterials.2015.07.043.

[38] M. Qiu, Y. Tang, J. Chen, R. Muriph, Z. Ye, C. Huang, J. Evans, E.P. Henske, Q. Xu, Lung-selective mRNA delivery of synthetic lipid nanoparticles for the treatment of pulmonary lymphangioleiomyomatosis, Proc. Natl. Acad. Sci. USA 119 (2022), e2116271119, https://doi.org/10.1073/pnas.2116271119.

[39] A.W. Dunn, V.V. Kalinichenko, D. Shi, Highly efficient in vivo targeting of the pulmonary endothelium using novel modifications of polyethylenimine: an importance of charge, Adv. Healthc. Mater. 7 (2018), 1800876, https://doi.org/10.1002/adhm.201800876.

[40] F. Kohram, Z. Deng, Y. Zhang, A.A. Al Reza, E. Li, O.A. Kolesnichenko, S. Shukla, V. Ustiyan, J. Gomez-Arroyo, A. Acharya, D. Shi, V. Kalinichenko, A.P. Kenny, Demonstration of safety in wild type mice of npFOXF1, a novel nanoparticle-based gene therapy for alveolar capillary dysplasia with misaligned pulmonary veins, Biol. Targets & Ther. 17 (2023) 43–55, https://doi.org/10.2147/BTT.S400006.

[41] Y. Liu, Y. Li, D. Keskin, L. Shi, Poly(β-Amino esters): synthesis, formulations, and their biomedical applications, Adv. Healthc. Mater. 8 (2018), 1801359, https://doi.org/10.1002/adhm.201801359.

[42] P. Mastorakos, A.L.D. Silva, J. Chisholm, E. Song, W.K. Choi, M.P. Boyle, M. M. Morales, J. Hanes, J.S. Suk, Highly compacted biodegradable DNA nanoparticles capable of overcoming the mucus barrier for inhaled lung gene therapy, Proc. Natl. Acad. Sci. U. S. A. 112 (2015) 8720–8725, https://doi.org/10.1073/pnas.1502281112.

[43] A. Dunn, D. Shi, Polymeric vectors for strategic delivery of nucleic acids, Nano Life 7 (2017), 1730003, https://doi.org/10.1142/s1793984417300035.

[44] J. Donovan, Z. Deng, F. Bian, S. Shukla, J. Gomez-Arroyo, D. Shi, V. V. Kalinichenko, T.V. Kalin, Improving anti-tumor efficacy of low-dose Vincristine in rhabdomyosarcoma via the combination therapy with FOXM1 inhibitor RCM1, Front. Oncol. 13 (2023) 1–14, https://doi.org/10.3389/fonc.2023.1112859.

[45] S. Liu, Y. Gao, D. Zhou, M. Zeng, F. Alshehri, R. Newland, J. Lyu, J. O'Keeffe-Ahern, U. Greiser, T. Guo, F. Zhang, W. Wang, Highly branched poly(β-amino ester) delivery of minicircle DNA for transfection of neurodegenerative disease related cells, Nat. Commun. 10 (2019), https://doi.org/10.1038/s41467-019-11190-0.

[46] M. Keeney, S.-G. Ong, A. Padilla, Z. Yao, S. Goodman, J.C. Wu, F. Yang, Development of poly(β-amino ester)-based biodegradable nanoparticles for nonviral delivery of minicircle DNA, ACS Nano 7 (2013) 7241–7250, https://doi.org/10.1021/nn402657d.

[47] J. Zhao, P. Huang, Z. Wang, Y. Tan, X. Hou, L. Zhang, C.-Y. He, Z.-Y. Chen, Synthesis of amphiphilic poly(β-amino ester) for efficiently minicircle DNA delivery in vivo, ACS Appl. Mater. Interfaces 8 (2016) 19284–19290, https://doi.org/10.1021/acsami.6b04412.

[48] F. Bian, Y.-W. Lan, S. Zhao, Z. Deng, S. Shukla, A. Acharya, J. Donovan, T. Le, D. Milewski, M. Bacchetta, A.E. Hozain, Y. Tipograf, Y.-W. Chen, Y. Xu, D. Shi, V. V Kalinichenko, T. V Kalin, Lung endothelial cells regulate pulmonary fibrosis through FOXF1/R-Ras signaling, Nat. Commun. 14 (2023) 2560, https://doi.org/10.1038/s41467-023-38177-2.

[49] J.C. Kaczmarek, A.K. Patel, K.J. Kauffman, O.S. Fenton, M.J. Webber, M. W. Heartlein, F. DeRosa, D.G. Anderson, Polymer–lipid nanoparticles for systemic delivery of mRNA to the lungs, Angew. Chem. Int. Ed. 55 (2016) 13808–13812, https://doi.org/10.1002/anie.201608449.

[50] J.C. Kaczmarek, K.J. Kauffman, O.S. Fenton, K. Sadtler, A.K. Patel, M.W. Heartlein, F. DeRosa, D.G. Anderson, Optimization of a degradable polymer-lipid nanoparticle for potent systemic delivery of mRNA to the lung endothelium and immune cells, Nano Lett. 18 (2018) 6449–6454, https://doi.org/10.1021/acs.nanolett.8b02917.

[51] J.C. Kaczmarek, A.K. Patel, L.H. Rhym, U.C. Palmiero, B. Bhat, M.W. Heartlein, F. DeRosa, D.G. Anderson, Systemic delivery of mRNA and DNA to the lung using polymer-lipid nanoparticles, Biomaterials 275 (2021) 120966, https://doi.org/10.1016/j.biomaterials.2021.120966.

[52] A.K. Patel, J.C. Kaczmarek, S. Bose, K.J. Kauffman, F. Mir, M.W. Heartlein, F. DeRosa, R. Langer, D.G. Anderson, Inhaled nanoformulated mRNA polyplexes for protein production in lung Epithelium, Adv. Mater. 31 (2019), 1805116, https://doi.org/10.1002/adma.201805116.

[53] M.K. Grun, A. Suberi, K. Shin, T. Lee, V. Gomerdinger, Z.M. Moscato, A. S. Piotrowski-Daspit, W.M. Saltzman, PEGylation of poly(amine-co-ester) polyplexes for tunable gene delivery, Biomaterials 272 (2021), 120780, https://doi.org/10.1016/j.biomaterials.2021.120780.

[54] J. Lv, H. Wang, G. Rong, Y. Cheng, Fluorination promotes the cytosolic delivery of genes, proteins, and peptides, Acc. Chem. Res. 55 (2022) 722–733, https://doi.org/10.1021/acs.accounts.1c00766.

[55] F. Tang, Q. Wang, Y. Gao, Y. Zhang, Y. Liang, Z. Lu, R. Liu, A. Ding, A NIR aggregation-induced emission fluoroamphiphile as visually trackable and serum-tolerant nonviral gene carrier, Bioconjugate Chem. 33 (2022) 929–937, https://doi.org/10.1021/acs.bioconjchem.2c00140.

[56] X. Cai, R. Jin, J. Wang, D. Yue, Q. Jiang, Y. Wu, Z. Gu, Bioreducible fluorinated peptide dendrimers capable of circumventing various physiological barriers for highly efficient and safe gene delivery, ACS Appl. Mater. Interfaces 8 (2016) 5821–5832, https://doi.org/10.1021/acsami.5b11545.

[57] Z. Yuan, X. Guo, M. Wei, Y. Xu, Z. Fang, Y. Feng, W.-E. Yuan, Novel fluorinated polycationic delivery of anti-VEGF siRNA for tumor therapy, NPG Asia Mater. 12 (2020) 34, https://doi.org/10.1038/s41427-020-0216-9.

[58] X. Wang, G. Rong, J. Yan, D. Pan, L. Wang, Y. Xu, M. Yang, Y. Cheng, In vivo tracking of fluorinated polypeptide gene carriers by positron emission tomography imaging, ACS Appl. Mater. Interfaces 12 (2020) 45763–45771, https://doi.org/10.1021/acsami.0c11967.

[59] M. Liu, Q. Li, L. Liang, J. Li, K. Wang, J. Li, M. Lv, N. Chen, H. Song, J. Lee, J. Shi, L. Wang, R. Lal, C. Fan, Real-Time visualization of clustering and intracellular transport of gold nanoparticles by correlative imaging, Nat. Commun. 8 (2017) 1–10, https://doi.org/10.1038/ncomms15646.

[60] L. Zhang, L. Zhang, LIPID–POLYMER hybrid nanoparticles: synthesis, characterization and applications, Nano Life 1 (2010) 163–173, https://doi.org/10.1142/S179398441000016X.

[61] Y. He, G. Jiang, T. Dong, L. Yang, X. Li, Stimulus-responsive mechanism of salt-responsive polymer and its application in saturated saltwater drilling fluid, Petrol. Explor. Dev. 47 (2020) 1131–1137, https://doi.org/10.1016/S1876-3804(20)60123-9.

[62] S. Xie, B. Zhang, Y. Mao, L. He, K. Hong, F.S. Bates, T.P. Lodge, Influence of added salt on chain conformations in poly(ethylene oxide) melts: SANS analysis with complications, Macromolecules 53 (2020) 7141–7149, https://doi.org/10.1021/acs.macromol.0c01194.

[63] A. Gillich, F. Zhang, C.G. Farmer, K.J. Travaglini, S.Y. Tan, M. Gu, B. Zhou, J. A. Feinstein, M.A. Krasnow, R.J. Metzger, Capillary cell-type specialization in the alveolus, Nature 586 (2020) 785–789, https://doi.org/10.1038/s41586-020-2822-7.

[64] G. Wang, B. Wen, Z. Deng, Y. Zhang, O.A. Kolesnichenko, V. Ustiyan, A. Pradhan, T.V. Kalin, V.V. Kalinichenko, Endothelial progenitor cells stimulate neonatal lung angiogenesis through FOXF1-mediated activation of BMP9/ACVRL1 signaling, Nat. Commun. 13 (2022) 2080, https://doi.org/10.1038/s41467-022-29746-y.

[65] C. Wu, J. Li, W. Wang, P.T. Hammond, Rationally designed polycationic carriers for potent polymeric siRNA-mediated gene silencing, ACS Nano 12 (2018) 6504–6514, https://doi.org/10.1021/acsnano.7b08777.

[66] Z. Zhang, N. Qiu, S. Wu, X. Liu, Z. Zhou, J. Tang, Y. Liu, R. Zhou, Y. Shen, Dose-Independent transfection of hydrophobized polyplexes, Adv. Mater. 33 (2021), 2102219, https://doi.org/10.1002/adma.202102219.

[67] J.S. Suk, Q. Xu, N. Kim, J. Hanes, L.M. Ensign, PEGylation as a strategy for improving nanoparticle-based drug and gene delivery, Adv. Drug Deliv. Rev. 99 (2016) 28–51, https://doi.org/10.1016/j.addr.2015.09.012.

[68] A.E. Nel, L. Mädler, D. Velegol, T. Xia, E.M.V. Hoek, P. Somasundaran, F. Klaessig, V. Castranova, M. Thompson, Understanding biophysicochemical interactions at the nano-bio interface, Nat. Mater. 8 (2009) 543–557, https://doi.org/10.1038/nmat2442.

[69] E. Blanco, H. Shen, M. Ferrari, Principles of nanoparticle design for overcoming biological barriers to drug delivery, Nat. Biotechnol. 33 (2015) 941–951, https://doi.org/10.1038/nbt.3330.

[70] J. Mosayebi, M. Kiyasatfar, S. Laurent, Synthesis, functionalization, and design of magnetic nanoparticles for theranostic applications, Adv. Healthc. Mater. 6 (2017), 1700306, https://doi.org/10.1002/adhm.201700306.

[71] F.M. Kievit, M. Zhang, Surface engineering of iron oxide nanoparticles for targeted cancer therapy, Acc. Chem. Res. 44 (2011) 853–862, https://doi.org/10.1021/ar2000277.

[72] J. Qiu, Q. Fan, S. Xu, D. Wang, J. Chen, S. Wang, T. Hu, X. Ma, Y. Cheng, L. Xu, A fluorinated peptide with high serum- and lipid-tolerance for the delivery of siRNA drugs to treat obesity and metabolic dysfunction, Biomaterials 285 (2022), 121541, https://doi.org/10.1016/j.biomaterials.2022.121541.

[73] L. Xue, Y. Yan, P. Kos, X. Chen, D.J. Siegwart, PEI fluorination reduces toxicity and promotes liver-targeted siRNA delivery, Drug Deliv. Transl. Res. 11 (2021) 255–260, https://doi.org/10.1007/s13346-020-00790-9.

[74] G. Chen, K. Wang, P. Wu, Y. Wang, Z. Zhou, L. Yin, M. Sun, D. Oupický, Development of fluorinated polyplex nanoemulsions for improved small interfering RNA delivery and cancer therapy, Nano Res. 11 (2018) 3746–3761, https://doi.org/10.1007/s12274-017-1946-z.

[75] C. Ge, J. Yang, S. Duan, Y. Liu, F. Meng, L. Yin, Fluorinated α-helical polypeptides synchronize mucus permeation and cell penetration toward highly efficient pulmonary siRNA delivery against acute lung injury, Nano Lett. 20 (2020) 1738–1746, https://doi.org/10.1021/acs.nanolett.9b04957.

[76] Q. Qiao, X. Liu, T. Yang, K. Cui, L. Kong, C. Yang, Z. Zhang, Nanomedicine for acute respiratory distress syndrome: the latest application, targeting strategy, and rational design, Acta Pharm. Sin. B. 11 (2021) 3060–3091, https://doi.org/10.1016/j.apsb.2021.04.023.

[77] L. Fu, H.N. Kim, J.D. Sterling, S.M. Baker, M.S. Lord, The role of the cell surface glycocalyx in drug delivery to and through the endothelium, Adv. Drug Deliv. Rev. 184 (2022), https://doi.org/10.1016/j.addr.2022.114195.

[78] J.A.K. Howard, V.J. Hoy, D. O'Hagan, G.T. Smith, How good is fluorine as a hydrogen bond acceptor? Tetrahedron 52 (1996) 12613–12622, https://doi.org/10.1016/0040-4020(96)00749-1.

[79] J. Lv, H. Wang, G. Rong, Y. Cheng, Fluorination promotes the cytosolic delivery of genes, proteins, and peptides, Acc. Chem. Res. 55 (2022) 722–733, https://doi.org/10.1021/acs.accounts.1c00766.

[80] M. Zoulikha, Q. Xiao, G.F. Boafo, M.A. Sallam, Z. Chen, W. He, Pulmonary delivery of siRNA against acute lung injury/acute respiratory distress syndrome, Acta Pharm. Sin. B. (2021), https://doi.org/10.1016/j.apsb.2021.08.009.

[81] Q. Dai, Y. Yan, C.S. Ang, K. Kempe, M.M.J. Kamphuis, S.J. Dodds, F. Caruso, Monoclonal antibody-functionalized multilayered particles: targeting cancer cells in the presence of protein coronas, ACS Nano 9 (2015) 2876–2885, https://doi.org/10.1021/nn506929e.

[82] D. Ding, Y. Zhang, E.A. Sykes, L. Chen, Z. Chen, W. Tan, The influence of physiological environment on the targeting effect of aptamer-guided gold nanoparticles, Nano Res. 12 (2019) 129–135, https://doi.org/10.1007/s12274-018-2191-9.

[83] J. Zhao, S. Wu, J. Qin, D. Shi, Y. Wang, Electrical-charge-mediated cancer cell targeting via protein corona-decorated superparamagnetic nanoparticles in a simulated physiological environment, ACS Appl. Mater. Interfaces 10 (2018) 41986–41998, https://doi.org/10.1021/acsami.8b15098.